

# Journal of Geophysical Research: Oceans

## RESEARCH ARTICLE

10.1029/2018JC014146

**Key Points:**

- A MATLAB toolbox, S\_TIDE, is used to realize enhanced harmonic analysis (EHA) for nonstationary tides
- S\_TIDE can separate oscillations in MWL, amplitudes, and phases on different time scales within a given frequency band using different number of IPs
- For D<sub>4</sub> constituents, not only the time variations but also the along-channel variations are dominated by river flow

**Supporting Information:**

- Supporting Information S1

**Correspondence to:**

X. Lv and H. Chen,  
xqinglev@ouc.edu.cn;  
chenhb2015@qdio.ac.cn

**Citation:**

Pan, H., Lv, X., Wang, Y., Matte, P., Chen, H., & Jin, G. (2018). Exploration of tidal-fluvial interaction in the Columbia River estuary using S\_TIDE. *Journal of Geophysical Research: Oceans*, 123. <https://doi.org/10.1029/2018JC014146>

Received 3 MAY 2018

Accepted 18 AUG 2018

Accepted article online 28 AUG 2018

## Exploration of Tidal-Fluvial Interaction in the Columbia River Estuary Using S\_TIDE

Haidong Pan<sup>1,2</sup>, Xianqing Lv<sup>1,2</sup> , Yingying Wang<sup>1,2</sup>, Pascal Matte<sup>3</sup> , Haibo Chen<sup>2,4</sup>, and Guangzhen Jin<sup>1,5</sup>

<sup>1</sup>Key Laboratory of Physical Oceanography, Qingdao Collaborative Innovation Center of Marine Science and Technology, Ocean University of China, Qingdao, China, <sup>2</sup>Qingdao National Laboratory for Marine Science and Technology, Qingdao, China, <sup>3</sup>Meteorological Research Division, Environment and Climate Change Canada, Quebec City, Quebec, Canada, <sup>4</sup>Key Laboratory of Ocean Circulation and Waves, Institute of Oceanology, Chinese Academy of Sciences, Qingdao, China, <sup>5</sup>Key Laboratory of Marine Resources and Coastal Engineering in Guangdong Province, School of Marine Sciences, Sun Yat-sen University, Guangzhou, China

**Abstract** Numerous tidal phenomena, including river tides, internal tides, and tides in ice-covered bay, are nonstationary, which pose a great challenge for traditional tidal analysis methods. Based on the independent point scheme and cubic spline interpolation, a new approach, namely the enhanced harmonic analysis, is developed to deal with nonstationary tides. A MATLAB toolbox, S\_TIDE, developed from the widely used T\_TIDE, is used to realize the approach. The efficiency of S\_TIDE is validated by analyzing a set of hourly water level observations from stations on the lower Columbia River. In all stations, the hindcast of S\_TIDE is more accurate than NS\_TIDE that is a powerful nonstationary tidal analysis tool adapted to river tides. The changing mean water level and tidal constituent properties obtained by S\_TIDE are similar to those obtained by NS\_TIDE, continuous wavelet transform, and empirical mode decomposition and highly consistent with theory on river tides. Moreover, different from NS\_TIDE that only can be applied to river tides, enhanced harmonic analysis is free of dynamic content, assuming only known tidal frequencies. Therefore, S\_TIDE can be applied to all kinds of nonstationary tides theoretically. Though powerful, S\_TIDE also has some limitations: S\_TIDE cannot be used for prediction and too many independent points in S\_TIDE may induce computational memory overflow and unrealistic results.

**Plain Language Summary** Based on the independent point scheme and cubic spline interpolation, a new approach, enhanced harmonic analysis, was developed to deal with nonstationary tides. Enhanced harmonic analysis is realized by a MATLAB toolbox, S\_TIDE, which is developed from the widely used T\_TIDE. S\_TIDE assumes only known tidal frequencies and theoretically can be applied to all kinds of nonstationary tides and stationary tides. In this study, S\_TIDE is applied to analyzing records of river tides that is one of the simplest kinds of nonstationary tides for which ample data are available. The method is compared with other methods to show its efficiency.

### 1. Introduction

As one of the most widely used methods for tidal elevations, classical harmonic analysis (HA) determines the amplitude and phase of a priori known frequency (derived from astronomical and hydrodynamic theory) via ordinary least squares regression. HA originally assumed that water levels are only affected by the tides, and that the tides are perfectly stationary, that is, *the music of the spheres* (Hoitink & Jay, 2016). However, in fact, all tidal time series are theoretically nonstationary. Nontidal perturbations like wind, waves, storm surge, and ice cover can induce nonstationary component in observations. Fortunately, in most coastal tidal elevation observations, the nonstationary components are extremely small and the tides can be considered nearly stationary. Thus, HA performs very well in tidal observations, usually over 95% of the variance can be explained by fewer than 150 constituents. But there are many tidal processes highly influenced by nontidal perturbations, including river tides, internal tides, and tides in ice-covered bay (Jay & Flinchem, 1999). In these circumstances, HA performs badly because of the unrealistic stationary assumption. For instance, for river tides, water level hindcast and predictions using classical HA can be in error by several meters (Hoitink & Jay, 2016).

For highly nonstationary tidal data, classical HA only provides mean values of time-dependent tidal properties, but no insight into the interactions of tidal and nontidal processes. To obtain insights into

underlying dynamics on nonstationary tidal data, several methods have been employed (Jay & Kukulka, 2003). These methods, such as complex demodulation, continuous wavelet transform (CWT), and short-term HA, can present varying amplitudes in time and frequency domains that reflect the influence of nontidal processes, but the resolution of constituents within a tidal band is limited (Matte et al., 2013). Also, these methods cannot define the subtidal oscillations that are important in nonstationary tides (e.g., river tides, Hoitink & Jay, 2016).

Matte et al. (2013, 2014) developed a nonstationary tidal analysis tool, NS\_TIDE, for river tides by modifying T\_TIDE (Pawlowicz et al., 2002) on the basis of the stage and tidal-fluvial models proposed by Kukulka and Jay (2003a, 2003b) and Jay et al. (2011). NS\_TIDE performs far better than classical HA for river tides, with an increased resolution of constituents within a tidal band compared to CWT. It uses a robust regression (Huber, 1996; Leffler & Jay, 2009) and builds the nonstationary forcing by river discharge and ocean tidal range directly into the HA basis functions. Therefore, it can reveal the influence of river flow and tidal forcing on mean water level (MWL) as well as temporal variations of tidal amplitudes and phases in a quantitative manner. However, despite its predictive capabilities, NS\_TIDE has two limitations: (i) absence of precise river discharge data restricts its usage; (ii) being specifically adapted to the analysis of river tides it cannot be applied to nonstationary tides with other dynamic mechanisms, such as, for example, internal tides.

Based on the independent point (IP) scheme and cubic spline interpolation, Jin et al. (2018) developed the enhanced harmonic analysis (EHA) and applied this algorithm to internal tidal currents in the South China Sea to determine the harmonic parameters with temporal variations. But internal tides are very complicated and relevant observations are extremely limited, these all impede the EHA algorithm. Thus, Jin et al. (2018) did not clarify how to select IP numbers for EHA and they also could not provide an explanation of the physical processes driving the temporal variations observed in the moored current data. In this paper, EHA is implemented in a MATLAB toolbox, S\_TIDE, which is developed from the widely used T\_TIDE. Then, to demonstrate the utility of S\_TIDE, we apply it to river tides to allow a comparative assessment with NS\_TIDE, and because river tides are conceptually the simplest nonstationary tidal process, for which both ample data and detailed theoretical analysis are available (Jay & Flinchem, 1997).

The paper is arranged as follows. Study area and data are described in section 2. In section 3, S\_TIDE is applied to analyzing water level records at Vancouver station and compared with T\_TIDE, CWT, empirical mode decomposition (EMD), and NS\_TIDE to show its efficiency. In section 4.1, other stations in the lower Columbia River (LCR) are also analyzed to evaluate our method and study the along-channel tidal-fluvial processes. Advantages and disadvantages of S\_TIDE are discussed in section 4.2. Conclusions in section 5 complete the paper. Appendix A presents the theoretical models of river tides. Appendix B presents the computation of cubic spline interpolation weights. Appendix C compares the performance of cubic spline interpolation with the linear interpolation.

## 2. Study Site and Data

### 2.1. Study Site

The Columbia River enters the northeast Pacific Ocean 30 km seaward of the Tongue Point tide gauge at Astoria, Oregon. As the third largest river in the United States, it has an annual average discharge of  $\sim 7,300 \text{ m}^3/\text{s}$  and a watershed of  $\sim 660,500 \text{ km}^2$  (Bottom et al., 2005). The LCR spans 235 river kilometers (rkm) from the mouth to the Bonneville Dam (Figure 1a). Its largest tributary, the Willamette River, enters the river main stem at Portland, 160 rkm from the ocean, with an average discharge of  $950 \text{ m}^3/\text{s}$  (Matte et al., 2013). The tides in the Columbia River Estuary have a mixed diurnal ( $D_1$ ) and semidiurnal ( $D_2$ ) feature with a  $D_2/D_1$  ratio of 1.8 at the estuary mouth (Jay et al., 2011). The diurnal tidal range in the LCR varies from  $\sim 1.7$  to  $3.6 \text{ m}$  at the ocean entrance and increases to a maximum of  $\sim 2.0$  to  $4.0 \text{ m}$ , at Astoria (rkm 29, Moftakhari et al., 2016). Tides propagate landward with amplitude decreasing monotonically, and they are virtually negligible at Bonneville dam (rkm 235), although power peaking from Bonneville dam is responsible for diel and weekly fluctuations propagating seaward (Jay et al., 2011, 2015). Furthermore, estuarine water levels are influenced by coastal upwelling and downwelling. As indicated by MacMahan (2016), in the Columbia River estuary, oceanic downwelling-induced subtidal fluctuations propagate upstream with small amplitude decrease, the relative oceanic subtidal motions represent 90% of the total subtidal contribution near the entrance that decrease to 40% at rkm 169.

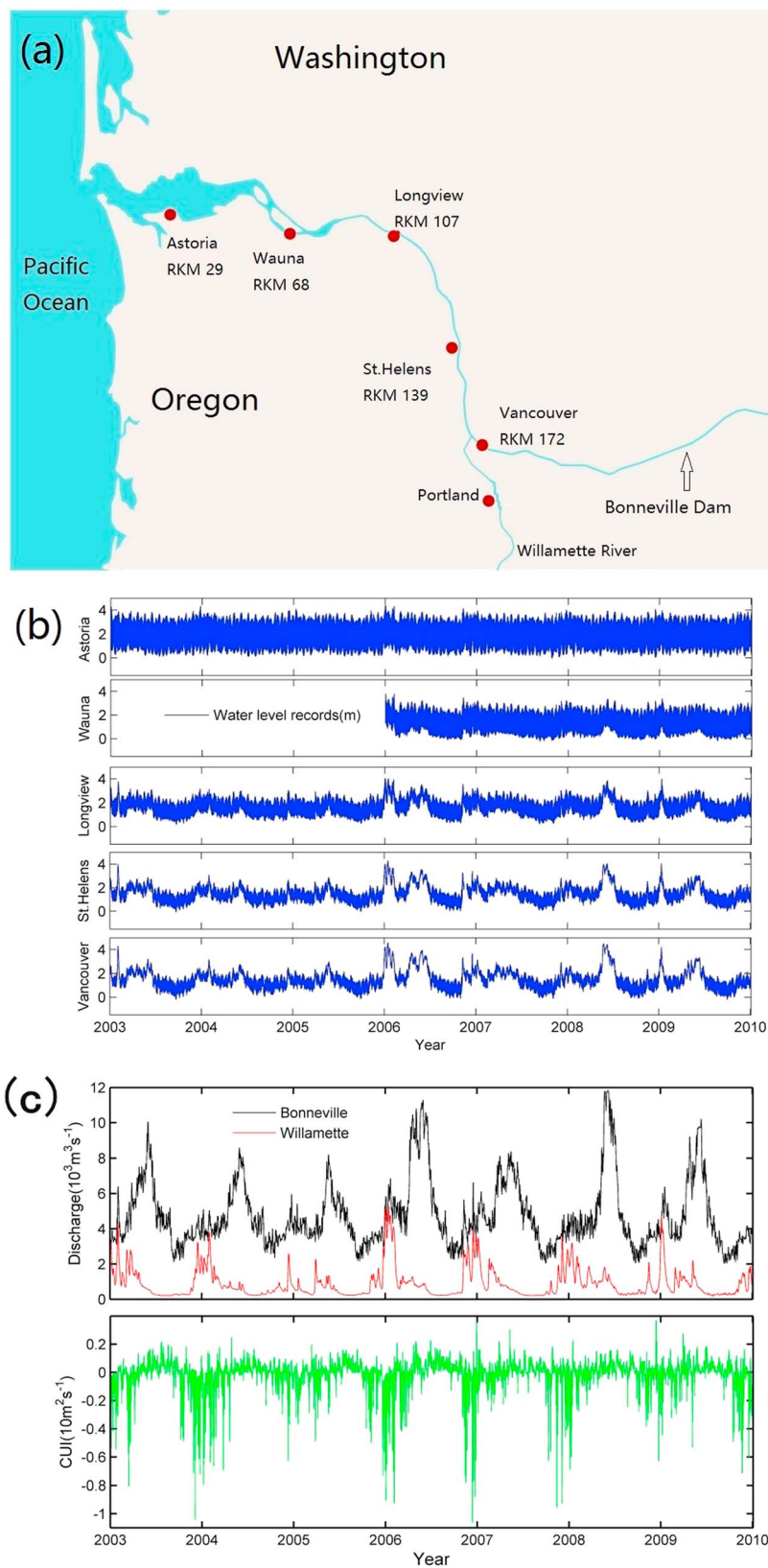


**Figure 1.** (a) Map of the lower Columbia River. (b) Water level records in the lower Columbia River. (c) River flow at the Bonneville dam (top) and in the Willamette River, (bottom) CUI at  $46^\circ\text{N}$ . CUI = Coastal Upwelling Index; rkm = river kilometers.

**Table 1**

Tidal Constituents at Vancouver With Amplitudes Greater Than 0.05 m and Overtide Constituents  $M_3$ ,  $M_4$ ,  $M_6$ , and  $M_8$

Tidal constituent	Amplitude (m)	Phase (deg)	Signal-to-noise ratio (SNR)
Sa	0.5905	276.07	53
Ssa	0.4419	319.12	21
Mm	0.0930	207.74	1.3
Msf	0.1586	247.54	2.8
O <sub>1</sub>	0.0702	204.63	380
K <sub>1</sub>	0.1204	15.85	1200
M <sub>2</sub>	0.2057	247.66	3400
M <sub>3</sub>	0.0019	3.17	1.2
M <sub>4</sub>	0.0385	54.46	470
M <sub>6</sub>	0.0035	232.04	230
M <sub>8</sub>	0.0004	129.45	11

## 2.2. Data

In this study, hourly water level observations for a 7-year period (January 2003 to December 2009) from Astoria (rm 29), Longview (rm 107), St. Helens (rm 139), and Vancouver (rm 172) in the LCR were studied (Figure 1a). Additional water level records at Wauna (rm 68) for a 4-year period (January 2006 to December 2009) were also studied. Tide and flow data were provided by the National Oceanic and Atmospheric Administration (<https://tidesandcurrents.noaa.gov/stations.html?type=Water+Levels>) and the U.S. Geological Survey (<https://nwis.waterdata.usgs.gov/nwis>). As shown in Figure 1b, water level variations at Astoria (rm 29) are nearly stationary. Water level variations at Wauna (rm 68) are similar to those at Astoria, but tides are slightly altered by discharge. Landward of Wauna, tides are obviously distorted and tidal range varies contrarily with river flow. At Longview (rm 107), St. Helens (rm 139), and Vancouver (rm 172), tides are greatly suppressed especially in the

high flow events and water levels are highly consistent with discharge. Finally, the effects of upwelling and downwelling can be represented by the offshore component of the Coastal Upwelling Index (CUI). The CUI data were obtained from National Oceanic and Atmospheric Administration (see <https://www.pfeg.noaa.gov/products/PFEL/modeled/indices/upwelling/> for further details). CUI values are interpolated between {45°N, 125°W} and {48°N, 125°W} to 46°N (near the mouth of the Columbia River, Jay et al., 2015).

## 3. Performance of Different Methods

### 3.1. Classical HA

In the classical HA method, water levels can be represented by a linear combination of sinusoidal terms (Foreman & Henry, 1989):

$$Z(t) = S_0 + \sum_{j=1}^J (H_j \cos(\sigma_j t - g_j)) \quad (1)$$

where  $Z(t)$  is the water level at time  $t$ .  $\sigma_j$ ,  $H_j$ , and  $g_j$  are the frequency, amplitude, and phase corresponding to the  $j$ th tidal constituent, respectively.  $S_0$  is the MWL. Equation (1) can be made linear in the new unknowns  $a_j$  and  $b_j$  by rewriting

$$Z(t) = S_0 + \sum_{j=1}^J (a_j \cos \sigma_j t + b_j \sin \sigma_j t) \quad (2)$$

where

$$H_j = \sqrt{a_j^2 + b_j^2}, \quad g_j = \arctan(b_j/a_j)$$

For use in regression analysis, equation (2) can be written in matrix form as  $\mathbf{Z} = \mathbf{Ax}$  where  $\mathbf{Z}$  is a vector of the water level,  $\mathbf{A}$  is a matrix of the basis functions evaluated at measurement times,  $\mathbf{x}$  is the unknown parameter vector. Classical HA is usually conducted using ordinary least squares, which gives each data point equal weight in the solution. To narrow the confidence intervals, a criterion is needed to restrict the number of constituents in the HA. Godin (1972) uses the Rayleigh separation equation

$$|\sigma_1 - \sigma_2| > \frac{1}{m\Delta t} \quad (3)$$

where  $\sigma_1$  and  $\sigma_2$  are two adjacent tidal frequencies,  $m$  is the number of samples,  $\Delta t$  is the sample interval, and  $m\Delta t$  is the length of record (LOR). After the minimal allowable frequency separation is determined by the Rayleigh criterion, tidal potential amplitude is used as a posterior to deciding the order of inclusion.

The classical HA (using T\_TIDE package) on the 7-year data from Vancouver extracts 63 significant constituents, of which the largest five constituents, Sa, Ssa, M<sub>2</sub>, Msf, and K<sub>1</sub> have amplitudes of 0.59, 0.44, 0.21, 0.16, and 0.12 m, respectively (Table 1). The dominant semidiurnal and diurnal constituents are M<sub>2</sub> and K<sub>1</sub>, respectively. The dominant overtide constituent, M<sub>4</sub>, is much smaller than the major diurnal and semidiurnal constituents. Note that nodal corrections are not included in the analyses because nodal modulations are

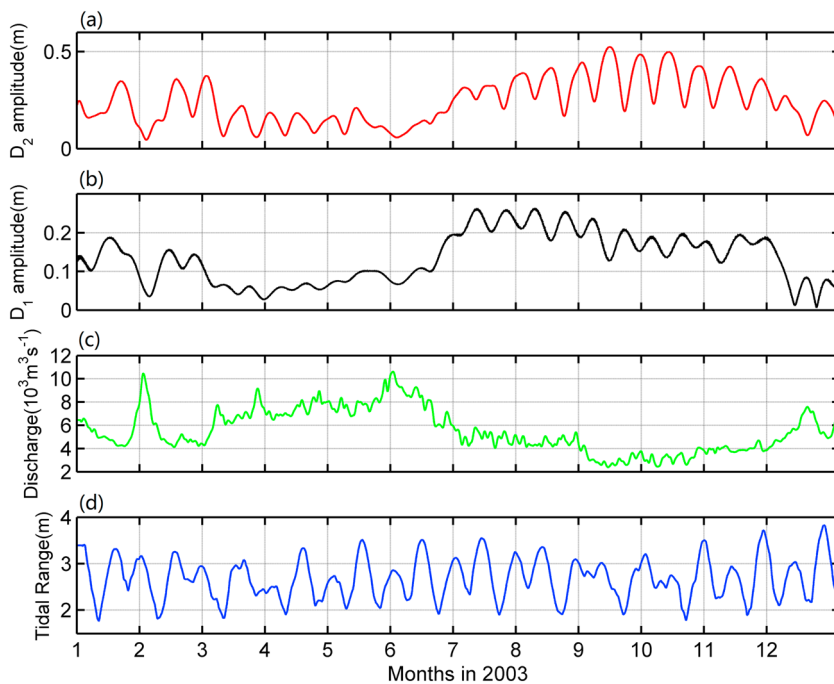


**Figure 2.** (a)  $D_2$  amplitude and (b)  $D_1$  amplitude obtained by CWT at Vancouver in 2003. Note the neap-spring cycle of  $\sim 15$  days. (c) Discharge in the lower Columbia River (sum of river flows at Bonneville dam and from the Willamette River). (d) Ocean tidal range forcing at Astoria. CWT = continuous wavelet transform.

usually small in river tides compared to the effects of stage variations (Matte et al., 2013). For comparison with results by T\_TIDE, nodal corrections are also not made to tidal properties determined by NS\_TIDE and S\_TIDE. T\_TIDE hindcast at Vancouver only explains 52.4% of the original signal variance, with a root-mean-square error (RMSE) of 1.60 m and a maximum absolute error (MAE) of 4.16 m for tidal heights. These results show the limitation of the classical HA to resolve nontidal perturbations associated with fluctuating river flow.

### 3.2. Wavelet Tidal Analysis

The wavelet transform is essentially an adjustable window Fourier transform with the following general definition:

$$W(a, b, x, \psi) = \int_{-\infty}^{\infty} x(t) \psi^* \left( \frac{t-b}{a} \right) dt \quad (4)$$

where  $x(t)$  is the input time series,  $\psi^*$  is the basic wavelet function,  $a$  is the frequency scale, and  $b$  is the translation of the origin. An intuitive physical interpretation of equation (4) is very simple:  $W(a, b, x, \psi)$  is the energy of  $x$  of scale  $a$  at time  $b$  (Huang et al., 1998). Like Jay and Flinchem (1997), we use CWTs for their flexibility. A Morlet-type wavelet function is used due to its optimal properties for tides (Guo et al., 2015; Hoitink & Jay, 2016; Losada et al., 2017; Sassi & Hoitink, 2013). Here we apply CWT to the 7-year data from Vancouver to extract the diurnal ( $D_1$ ) species amplitude and semidiurnal ( $D_2$ ) species amplitude (Figure 2). The change of  $D_1$  and  $D_2$  amplitude is consistent with the theoretical tidal-fluvial model (see Kukulka & Jay, 2003a; also see equations (A1)–(A3) in Appendix A). The  $D_1$  and  $D_2$  amplitudes are smaller when the discharge is larger. The  $D_1$  and  $D_2$  amplitudes also vary quasi-periodically with semimonthly neap-spring cycle due to frictional interactions. From July 2003 to November 2003, fortnightly oscillations in  $D_1$  and  $D_2$  amplitudes become stronger as the river flow decreases.

### 3.3. NS\_TIDE

#### 3.3.1. Introduction to NS\_TIDE

NS\_TIDE (Matte et al., 2013) assumes time-varying  $S_0$ ,  $a_j$ , and  $b_j$  by changing the constant model coefficients in equation (2) by functions of the river flow  $Q$  and greater diurnal tidal range  $R$  at the reference station (see Appendix A):

**Table 2**

Selected Constituents in NS\_TIDE for an 7-Year-Long Record (January 2003 to December 2009) at Vancouver

Tidal bands	Constituents ( $\eta = 0.15$ )
D1	SIG <sub>1</sub> , Q <sub>1</sub> , O <sub>1</sub> , NO <sub>1</sub> , K <sub>1</sub> , J <sub>1</sub> , SO <sub>1</sub> , and UPS <sub>1</sub>
D2	EPS <sub>2</sub> , MU <sub>2</sub> , N <sub>2</sub> , M <sub>2</sub> , L <sub>2</sub> , S <sub>2</sub> , and MSN <sub>2</sub>
D3	MO <sub>3</sub> , M <sub>3</sub> , MK <sub>3</sub> , and SK <sub>3</sub>
D4	MN <sub>4</sub> , M <sub>4</sub> , SN <sub>4</sub> , MS <sub>4</sub> , SK <sub>4</sub>
D5	2MK <sub>5</sub> and 2SK <sub>5</sub>
D6	2MN <sub>6</sub> , M <sub>6</sub> , 2MS <sub>6</sub> , and MSK <sub>6</sub>
D7	3MK <sub>7</sub>
D8	M <sub>8</sub>

$$Z(t) = S_{0,0} + \sum_{j=1}^J (S_{1,j} \cos \sigma_j t + S_{2,j} \sin \sigma_j t) \quad (5)$$

$$S_{l,j} = d_{0,l,j} + d_{1,l,j} Q^p + d_{2,l,j} \frac{R^q}{Q^r} \quad (6)$$

where  $l$  is index for coefficients ( $l = 0, 1, 2$ ).  $p$ ,  $q$ , and  $r$  are the exponents for the stage model (represented by  $S_{0,0}$ ) and the tidal-fluvial model (represented by the summation in equation (5)), whose theoretical values are given by Kukulka and Jay (2003a, 2003b). Matte et al. (2013) only considered the interactions of tides with river flow, while other important physical processes like upwelling and downwelling may significantly affect water levels (Jay et al., 2016).

In this paper, we use a newer version of NS\_TIDE in which the contribution from CUI can be added, in a way to mimic the regression models used by Jay et al. (2016) in the Columbia River, as shown below:

$$S_{l,j} = d_{0,l,j} + d_{1,l,j} Q_{\text{Bon}}^p + d_{2,l,j} Q_{\text{Wil}}^q + d_{3,l,j} \frac{R^q}{(Q_{\text{Bon}} + Q_{\text{Wil}})^r} + d_{4,l,j} \text{CUI} \quad (7)$$

where  $Q_{\text{Bon}}$  and  $Q_{\text{Wil}}$  represent river flows at Bonneville dam and from the Willamette River, respectively. With  $Q(t)$ ,  $R(t)$ ,  $\text{CUI}(t)$ , and  $Z(t)$  known, equation (5) can be solved via a fitting procedure. In NS\_TIDE, the iteratively reweighted least squares is implemented (Huber, 1996; Leffler & Jay, 2009).

The Rayleigh criterion (equation (3), Godin, 1972) is no longer valid for nonstationary tides. Munk et al. (1965) stated that the width of the cusps formed around the tidal spectral lines is related to the low-frequency spectrum of the nonlinear forcing. Starting from this fact, NS\_TIDE redefined the Rayleigh criterion for nonstationary tides by accounting for the smearing of the spectral energy of the major tidal constituents over closely spaced, smaller constituents:

$$|\sigma_1 - \sigma_2| > \max\left(\frac{1}{m\Delta t}, \Delta\sigma\right) \quad (8)$$

where  $\Delta\sigma$  is given by

$$\frac{\int_0^{\Delta\sigma} P(\sigma) d\sigma}{\int_0^\infty P(\sigma) d\sigma} = 1 - \eta \quad (9)$$

where  $P(\sigma)$  is the normalized spectrum of either  $Q^p$  or  $1/Q^r$ , and  $\eta$  is a user-defined criterion representing a fraction of its total spectral power. With fewer constituents (smaller  $\eta$ ) the overlap between frequencies is less, but the calculated amplitudes will include unknown contributions from nearby unresolved frequencies, and vice versa (Matte et al., 2013).

### 3.3.2. Application of NS\_TIDE to River Tides

As in Matte et al. (2013), the Astoria station (29 rkm) is chosen as the reference station in the LCR for the use in NS\_TIDE, because it is the most seaward station where sufficient data are available and it is weakly influenced by river flow. The parameter  $\eta$  for the redefined Rayleigh criterion is set at 0.15, similar to Matte et al. (2013), thus allowing 32 constituents (Table 2) to be included in NS\_TIDE for Vancouver station. Exponents in equation (7) are optimized using a built-in procedure, described in Matte et al. (2013). It should be noted that the constituents with low frequency, like MSf (semimonthly), Ssa (semiannual), and Sa (annual) are contained in changes of the MWL and are accounted for by the stage model; thus, they were not extracted separately by NS\_TIDE. Two nontidal constituents with periods of 3.5 and 7 days caused by hydroelectric operations (*power peaking*) are also accounted for by the stage model. The hindcast is made with constituents with a mean signal-to-noise ratio greater than 2, determined using a correlated noise model (Matte et al., 2013).

Results obtained by NS\_TIDE show a significant improvement over T\_TIDE at Vancouver station for the 2003–2009 period: Its hindcast accounts for 96.0% of the original signal variance with a RMSE of 0.155 m and a MAE of 1.018 m. The time-varying amplitudes of the M<sub>2</sub> and K<sub>1</sub> constituents obtained by NS\_TIDE at Vancouver are shown in Figure 3. Results from NS\_TIDE display oscillations in the M<sub>2</sub> and K<sub>1</sub> amplitudes and phases around their mean values following the variations in forcing. Amplitudes are significantly

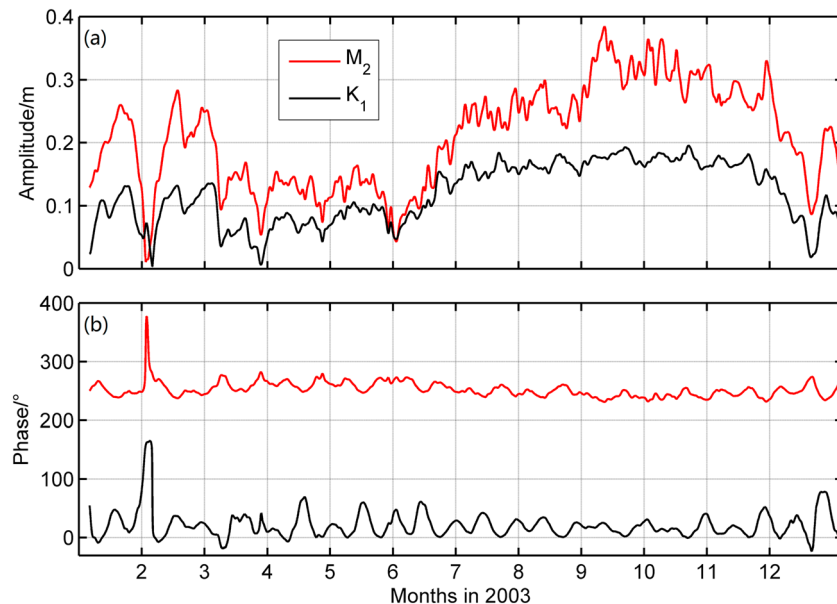


**Figure 3.** (a) M<sub>2</sub> and K<sub>1</sub> amplitudes obtained by NS\_TIDE at Vancouver station. (b) Same as Figure 3a but for phases.

reduced and phases shifted as the river flow increases (cf. Figure 2c). The K<sub>1</sub> and M<sub>2</sub> amplitudes and phases also vary quasi-periodically with semimonthly neap-spring cycle due to frictional interactions.

### 3.4. S\_TIDE

#### 3.4.1. Introduction to S\_TIDE

The newly proposed EHA also assumes time-varying  $S_0$ ,  $a_j$ , and  $b_j$  like NS\_TIDE:

$$Z(t) = S(t) + \sum_{j=1}^J (a_j(t) \cos \sigma_j t + b_j(t) \sin \sigma_j t) \quad (10)$$

But different from NS\_TIDE, equation (10) is solved with the IP scheme (Guo et al., 2017; Lu & Zhang, 2006; Pan et al., 2017; Zhang et al., 2011). The basic idea of the IP scheme is very simple: see Figure A1 for example. Assume harmonic parameters (e.g., amplitude) are time-varying, and  $X = \{x_1, x_2, x_3, \dots, x_9\}$  is the time indices. First, the indices of IPs, namely,  $\bar{X} = \{x_1, x_3, x_5, x_7, x_9\}$ , are selected as the representatives of the parameter space.  $\bar{X}$  is a subset of  $X$ . Second, the harmonic parameters at IPs (red circles in Figure A1) can be calculated through a specific algorithm (details are provided later). At last, harmonic parameters on the other points ( $x_2, x_4, x_6, x_8$ ) can be interpolated between the IPs (Jin et al., 2018).  $\bar{X}$  is named *independent points* because values at other points are obtained by interpolating values at IPs or, in some sense, they *depend* on values at IPs (Guo et al., 2018).

The main idea of EHA can be expressed in the following procedures. The MWL and tidal coefficients at IPs, which are uniformly distributed in the time domain, are selected as independent parameters (denoted as  $S_i$ ,  $a_{i,j}$ , and  $b_{i,j}$ ), and those at other points are obtained by interpolation between the IPs. Therefore, the changing MWL and tidal coefficients can be expressed by functions of  $S_i$ ,  $a_{i,j}$ , and  $b_{i,j}$ , which are

$$\begin{aligned} S(t) &= \sum_{i=1}^{M_s} f_{t,i} S_i \\ a_j(t) &= \sum_{i=1}^M f_{t,i} a_{i,j} \\ b_j(t) &= \sum_{i=1}^M f_{t,i} b_{i,j} \end{aligned} \quad (11)$$

where  $f_{t,i}$  is the interpolation weight for the  $i$ th IP at time  $t$ , which depends on the interpolation method.  $M_s$  and  $M$  are the IP numbers for MWL and constituents, respectively. It should be noted that the values of  $S_i$ ,  $a_{i,j}$ ,

and  $b_{ij}$  are unknown now, but through interpolation, the time-varying  $S(t)$ ,  $a_j(t)$ , and  $b_j(t)$  are expressed by linear combinations of the values of  $S_i$ ,  $a_{i,j}$ , and  $b_{i,j}$ , respectively (equation (11)). Combination of equations (10) and (11) yields equation (12)

$$Z(t) = \sum_{i=1}^{M_s} f_{t,i} S_i + \sum_{j=1}^J \left( \sum_{i=1}^M f_{t,i} a_{i,j} \cos \sigma_j t + \sum_{i=1}^M f_{t,i} b_{i,j} \sin \sigma_j t \right) \quad (12)$$

The cubic spline interpolation is widely implemented due to its stable, convergent, and smooth characteristics (Huang et al., 1998; Malik et al., 2011; Pan et al., 2017). Therefore, it is adopted in the present scheme. Refer to Appendix B for computation of cubic spline interpolation weights. With measurements at  $N$  moments, that is,  $Z = Z_1, Z_2, \dots, Z_N$  at  $t = t_1, t_2, \dots, t_N$ , we obtain the following equation set:

$$\begin{cases} \sum_{i=1}^{M_s} f_{t_1,i} S_i + \sum_{j=1}^J \left( \sum_{i=1}^M f_{t_1,i} a_{i,j} \cos \sigma_j t_1 + \sum_{i=1}^M f_{t_1,i} b_{i,j} \sin \sigma_j t_1 \right) = Z(t_1) \\ \sum_{i=1}^{M_s} f_{t_2,i} S_i + \sum_{j=1}^J \left( \sum_{i=1}^M f_{t_2,i} a_{i,j} \cos \sigma_j t_2 + \sum_{i=1}^M f_{t_2,i} b_{i,j} \sin \sigma_j t_2 \right) = Z(t_2) \\ \dots \\ \sum_{i=1}^{M_s} f_{t_N,i} S_i + \sum_{j=1}^J \left( \sum_{i=1}^M f_{t_N,i} a_{i,j} \cos \sigma_j t_N + \sum_{i=1}^M f_{t_N,i} b_{i,j} \sin \sigma_j t_N \right) = Z(t_N) \end{cases} \quad (13)$$

There are a total of  $2 MJ + M_s$  unknowns in equation (13), which can be estimated when  $N$ , the number of observation records, is much larger than  $2 MJ + M_s$ . Thereafter,  $S_i$ ,  $a_{i,j}$ , and  $b_{i,j}$  can be estimated via least squares fitting. Finally, the time-varying MWL and amplitudes and phase of each constituent can be obtained by interpolating  $S_i$ ,  $a_{i,j}$ , and  $b_{i,j}$ .

The error estimation algorithm can be expressed in the following steps (Jin et al., 2018). First, the tidal part and subtidal part estimated by EHA are removed from the original observed time series to obtain the residual or noise. Then, 300 synthetic noise realizations are generated by resampling the time series of residuals. Third, tidal part and subtidal parts are added back to each noise realization, from which new estimates of tidal part and subtidal part are obtained by means of least squares fit. Finally, the confidence intervals can be calculated using Student  $t$  distribution.

The selection of number of IPs will be discussed in detail in the next section. In S\_TIDE, constituent selection is dependent on the number of IPs. In section 3.4.3, we will show how the numbers of IPs influence the selection of constituents.

### 3.4.2. Sensitivity Experiments on the Number of IPs for MWL

We performed a series of sensitivity experiments, where the number of IPs for MWL increased gradually from 5 to 2000. In this section, tides are not included, equation (12) is simplified as

$$Z(t) = \sum_{i=1}^{M_s} f_{t,i} S_i \quad (14)$$

As the IP number increases, MWLs obtained by S\_TIDE show more oscillations (Figure 4). In fact, the MWLs obtained by S\_TIDE with different IP numbers represent oscillations on different time scales of MWL. We think S\_TIDE could play the role of a low-pass filter while the cutoff frequency depends on IP numbers. To further test our guess, we compare the results of S\_TIDE with those of EMD. The EMD method is extremely useful for nonstationary and nonlinear time series and has been widely applied to different kinds of geophysical data (Cheng et al., 2016, 2017; Ezer, 2013; Ezer & Corlett, 2012; Ezer et al., 2016; Pan et al., 2018). Assuming that nonstationary signals are composed of oscillations on different time scales, the EMD method aims to extract these oscillations called intrinsic mode functions (Huang et al., 1998). Pan et al. (2018) adapted the EMD method to river tides to study the nonstationary characteristics of the D<sub>1</sub> tides, the D<sub>2</sub> tides, and the MWL induced by changing river flow. Like Pan et al. (2018), here, we decomposed the water level observations at Vancouver station with the EMD method and obtained 13 modes (see Figure S1 in the supporting materials.). The highest and second highest frequency modes of the EMD method represent the semidiurnal (D<sub>2</sub>) and diurnal (D<sub>1</sub>) tides, respectively (Pan et al., 2018). The averaged period of any intrinsic mode function component almost exactly doubles that of the previous one except for modes 12 and 13, indicating that EMD is a dyadic filter (Flandrin et al., 2004; Pan et al., 2018; Wu & Huang, 2004).

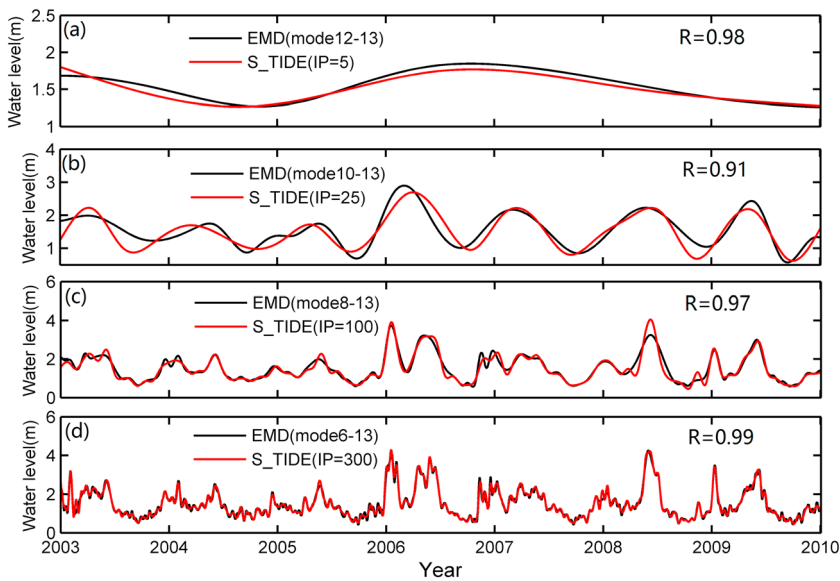


**Figure 4.** MWLs estimated by S\_TIDE with different number of IPs compared with modes obtained by EMD.  $R$  is the correlation coefficient between the results of EMD and S\_TIDE. MWLs = mean water levels; IP = independent point; EMD = empirical mode decomposition.

As shown in Figure 4, the results of S\_TIDE and EMD are highly consistent with each other, which indicate S\_TIDE can act as a low-pass filter to some extent. The MWL extracted by S\_TIDE with 5 IPs has a correlation coefficient of 0.98 with the combination of modes 12 and 13 obtained by EMD; the MWL extracted with 25 IPs has a correlation coefficient of 0.91 with the combination of modes 10–13; the MWL extracted with 100 IPs has a correlation coefficient of 0.97 with the combination of modes 8–13; the MWL extracted with 300 IPs has a correlation coefficient of 0.99 with the combination of modes 6–13.

As indicated by Pan et al. (2018), the sum of the third and higher EMD modes is MWL (Figure 5). The MWL extracted by S\_TIDE with 1,500 IPs has a correlation coefficient of 0.997 with the result of EMD. As displayed

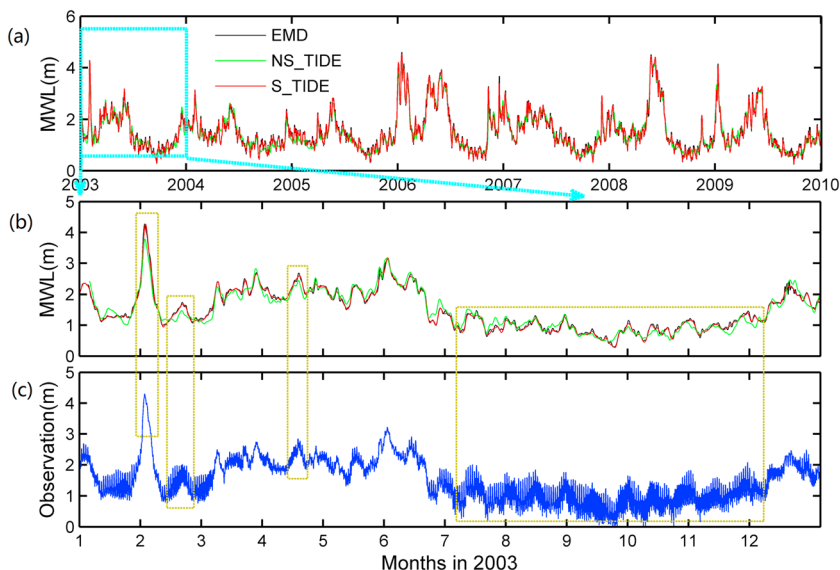


**Figure 5.** (a) MWLs obtained by EMD (mode 3–13), S\_TIDE ( $IP = 1,500$ ), and NS\_TIDE at Vancouver, from January 2003 to December 2009. (b) Same as Figure 5a but from January 2003 to December 2003. (c) Water level observations at Vancouver from January 2003 to December 2003. MWLs = mean water levels; EMD = empirical mode decomposition; IP = independent point.

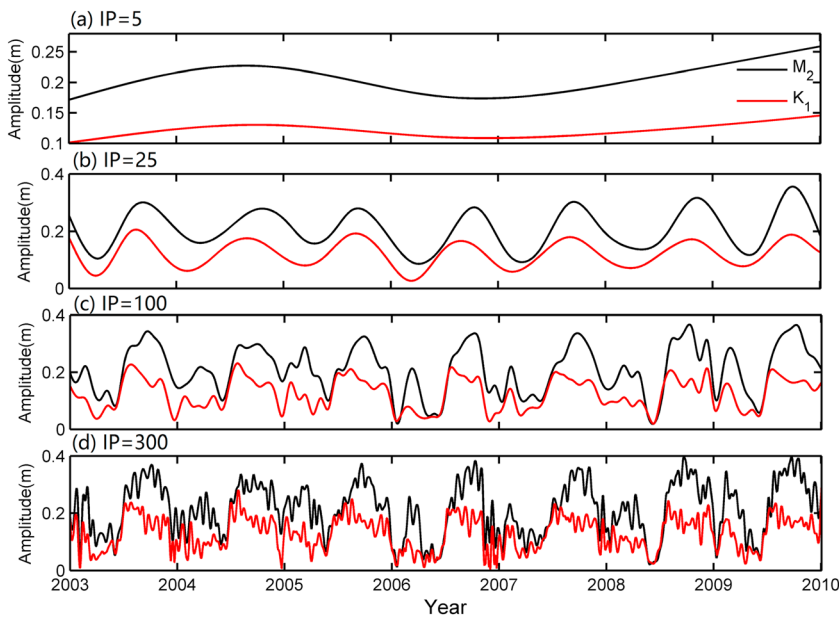


**Figure 6.**  $M_2$  and  $K_1$  amplitudes obtained by S\_TIDE at Vancouver with different IP numbers. IP = independent point.

in Figure 5a, MWLs obtained by the three methods (EMD, S\_TIDE, and NS\_TIDE) have a highly similar pattern. However, Figure 5b indicates that MWL obtained by NS\_TIDE seems slightly different from MWLs obtained by EMD and S\_TIDE; the peak values in MWLs obtained by NS\_TIDE are underestimated compared to those obtained by EMD and S\_TIDE. For example, in early February 2003, the water level raised significantly to 4.30 m due to the increase of discharge (Figure 5c). Peak values in MWLs obtained by EMD, S\_TIDE, and NS\_TIDE are 4.28, 4.27, and 3.78 m, respectively. Note that when the discharge is very large, amplitudes of tidal constituents decrease to extremely small values. Therefore, the peak values are mainly explained by changes in MWL and seem less accurate in NS\_TIDE than those obtained by EMD and S\_TIDE. One way to improve the results for NS\_TIDE would be to weigh the input discharge values based on their frequency of occurrence, similar to Jay et al. (2016), although we did not pursue this.

### 3.4.3. Sensitivity Experiments on the Number of IPs for Constituents

We also performed experiments to test the sensitivity of S\_TIDE to the IP number for tidal constituents. In this section, we only consider the constituents  $M_2$  and  $K_1$  and the IP numbers for MWL are set to 1,500.  $M_2$  and  $K_1$  amplitudes obtained by S\_TIDE at Vancouver with different IP numbers are shown in Figure 6. As the IP number increases, the amplitudes show more oscillations around the mean values. When the IP numbers increase to 400,  $M_2$  and  $K_1$  amplitudes obtained by S\_TIDE show clear semimonthly oscillations (Figure 7).

In fact, in this situation,  $M_2$  and  $K_1$  amplitudes obtained by S\_TIDE can be regarded as  $D_2$  and  $D_1$  amplitudes approximately (details are discussed later). As shown in Figure 7,  $D_2$  amplitudes obtained by S\_TIDE are similar to those obtained by CWT and NS\_TIDE. In the latter case, because multiple tidal constituents are resolved in each tidal band by NS\_TIDE (cf. Table 2), a band filter was used to produce the  $D_1$  and  $D_2$  amplitude time series, representing the total resolved energy in the diurnal and semidiurnal tidal bands, respectively.

Like MWL, we argue that the amplitudes and phases obtained by S\_TIDE with different IP numbers also represent oscillations on different time scales. Comparing Figures 4 and 6, we find that MWLs and amplitudes obtained by S\_TIDE with the same IP numbers are inversely related to each other (Table 3). This is consistent with the theory: when the river flow increases, then MWL also increases, whereas amplitudes of constituents decrease, indicating that the variations of MWL and constituent amplitude are systematically opposite at the analyzed station. It should be noted that

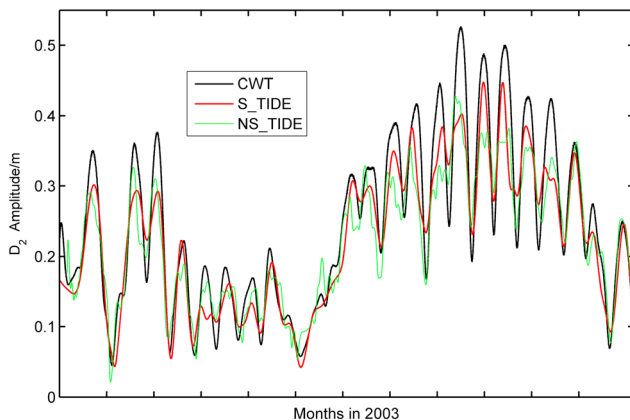


**Figure 7.**  $D_2$  amplitudes obtained by CWT, S\_TIDE (IP = 400), and NS\_TIDE at Vancouver. IP = independent point; CWT = continuous wavelet transform.

**Table 3**

The Correlation Coefficient Between MWLs and Amplitudes Obtained by S\_TIDE With the Same IP Numbers

IP number	5	25	100	300	400
MWL, M <sub>2</sub>	-0.95	-0.97	-0.95	-0.90	-0.81
MWL, K <sub>1</sub>	-0.93	-0.84	-0.78	-0.75	-0.62

Note. MWL = mean water level; IP = independent point.

here we do not consider other factors that may also contribute to changes in MWL, like sea level rise or channel deepening (Familkhali & Talke, 2016).

The oscillations on different time scales in MWL, amplitudes, and phases are definitely induced by the oscillations on different time scales in external forcing (in this study, river flow). To further test our guess, we decomposed the 7-year discharge record in the LCR (sum of river flows at Bonneville dam and from the Willamette River) with the EMD method

and obtained 11 modes (not shown). As indicated by Kukulka and Jay (2003a), the Columbia River flow shows interannual, annual, seasonal, and weekly variations. The combination of mode 10 and mode 11 obtained by EMD can be regarded as interannual variations in discharge approximately (Figure 8a). As shown in Figure 8a, interannual fluctuations in river flow are highly consistent with MWL but inversely related to M<sub>2</sub> amplitudes. Figure 8a indicates that the oscillations in MWL and M<sub>2</sub> amplitudes obtained by S\_TIDE with five IPs are likely induced by interannual fluctuations in river flow. The combination of modes 7–11 can be regarded as annual variations in discharge approximately (Figure 8b). As shown in Figure 8b, we can also conclude that the oscillations in MWL and M<sub>2</sub> amplitudes obtained by S\_TIDE with 25 IPs are mainly caused by annual fluctuations in river flow. It should be noted that the significant difference between the red line and green line at the end part shown in Figure 8b may be due to the end effect of the EMD method (Huang et al., 1998). Although S\_TIDE cannot quantify contributions of river flow and tidal forcing to MWL as well as tidal properties (amplitudes and phases), S\_TIDE can separate oscillations in MWL, amplitudes, and phases on different time scales (Figures 4 and 6). Furthermore, we can infer the characteristic time scales of river flow from the results obtained by S\_TIDE with different IP numbers.

As shown in Table 4, the performance of S\_TIDE can be improved as more IPs are adopted. It should be noted that the hindcast obtained by S\_TIDE with five IPs for constituents is still better than that by NS\_TIDE ( $\eta = 0.15$ ), accounting for 96.78% of the original signal variance and having a RMSE of 0.142 m and a MAE of 0.613 m. With five IPs for constituents, S\_TIDE only resolves the interannual variability for tidal constituents (Figure 8a), but the statistics are good because we use 1,500 IPs for MWL. The tides are relatively weak at Vancouver station; thus, the accurate inversion of MWL is the key for the good performance of S\_TIDE.

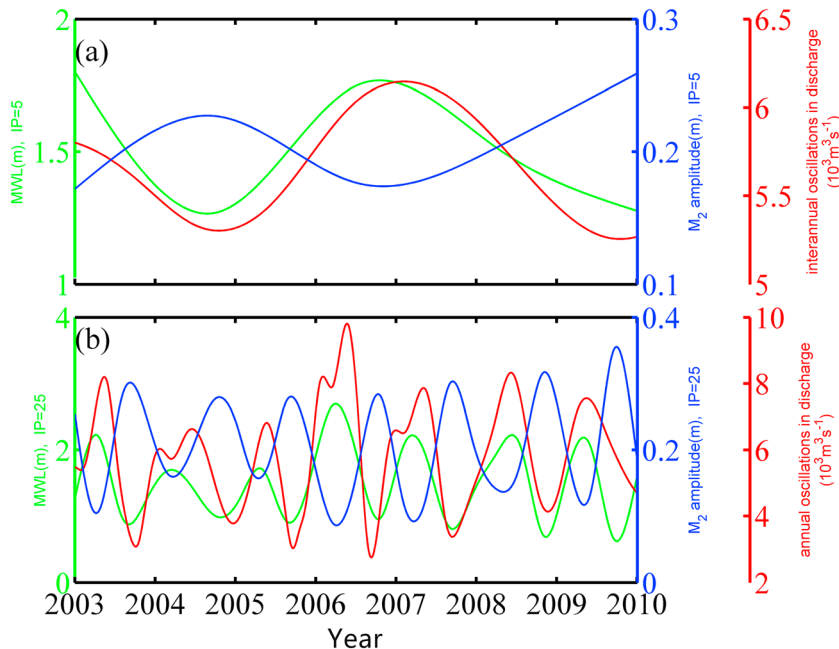


**Figure 8.** (a) MWL, M<sub>2</sub> amplitudes obtained by S\_TIDE with five IPs and interannual fluctuations in river flow obtained by EMD. (b) MWL, M<sub>2</sub> amplitudes obtained by S\_TIDE with 25 IPs and annual fluctuations in river flow obtained by EMD. MWL = mean water level; IPs = independent points; EMD = empirical mode decomposition.

**Table 4**

The Performance of S\_TIDE With Different IP Numbers for Major Constituents (IP Number for MWL Was Set to 1,500)

IP number	Percent variance (%)	RMSE (m)	MAE (m)
5	96.78	0.142	0.613
25	97.30	0.130	0.604
100	97.66	0.121	0.555
300	97.97	0.112	0.506
400	98.63	0.093	0.512

Note. Only considers M<sub>2</sub> and K<sub>1</sub>. MWL = mean water level; IP = independent point; RMSE = root-mean-square error; MAE = mean water level.

However, the participation of more IPs means more computation amount and time, but fewer constituents can be resolved. We use classical HA to reanalyze the hindcast obtained by S\_TIDE with different IP numbers for major constituents. As shown in Table S1 and Figure 9, as IP numbers increase, M<sub>2</sub> constituent inverted by S\_TIDE includes more contributions from nearby frequencies. When IP numbers increase to 400, M<sub>2</sub> nearly absorbs the energy of all major D<sub>2</sub> constituents (Figure 9) and K<sub>1</sub> nearly absorbs the energy of all major D<sub>1</sub> constituents (not shown). There is a trade-off between the number of constituents included in S\_TIDE and the numbers of IP for constituents. We can use more IPs for fewer constituents, which means the changes of tidal properties can be more complex, and vice versa.

The selection of IP number is not straightforward. For example, as shown in Table S1, if we adopt 25 IPs for M<sub>2</sub> in S\_TIDE, the M<sub>2</sub> obtained by S\_TIDE will absorb four nearby constituents (GAM<sub>2</sub>, H<sub>1</sub>, H<sub>2</sub>, and MKS<sub>2</sub>), which means those constituents cannot be resolved by S\_TIDE. However, in fact, the constituents near MKS<sub>2</sub> like LDA<sub>2</sub> and L<sub>2</sub> also cannot be resolved by S\_TIDE, though they are not absorbed into M<sub>2</sub>. This can be explained as follows: if we also adopt the IP scheme to resolve L<sub>2</sub>, L<sub>2</sub> will also absorb nearby constituents (e.g., MKS<sub>2</sub>, LDA<sub>2</sub>, T<sub>2</sub>, and S<sub>2</sub>). The scopes of M<sub>2</sub> and L<sub>2</sub> have an intersection (MKS<sub>2</sub>), and this intersection will induce wrong inversions of M<sub>2</sub> and L<sub>2</sub>. Thus, although we adopt fewer IPs for major constituents, the constituents we can resolve by S\_TIDE are still limited. If we want to resolved more constituents, the following equation can be adopted:

$$Z(t) = S(t) + \sum_{j=1}^J (a_j(t) \cos \sigma_j t + b_j(t) \sin \sigma_j t) + \sum_{k=1}^K (a_k \cos \sigma_k t + b_k \sin \sigma_k t) \quad (15)$$

Equation (15) means that J major constituents are extracted with the IP scheme, and K minor constituents are extracted with the classical HA. However, equation (15) assumes that minor constituents are stationary, which is unrealistic for river tides.

Jin et al. (2018) borrowed from the work of Matte et al. (2013) and redefined the Rayleigh criterion of EHA for nonstationary internal tides. But we now think the redefined Rayleigh criterion is insufficient because it has no regard for the selection of IP number. Therefore, the redefined Rayleigh criterion is used only a priori to select constituents to include in the analysis. Then we use the selected IP number and the significance of

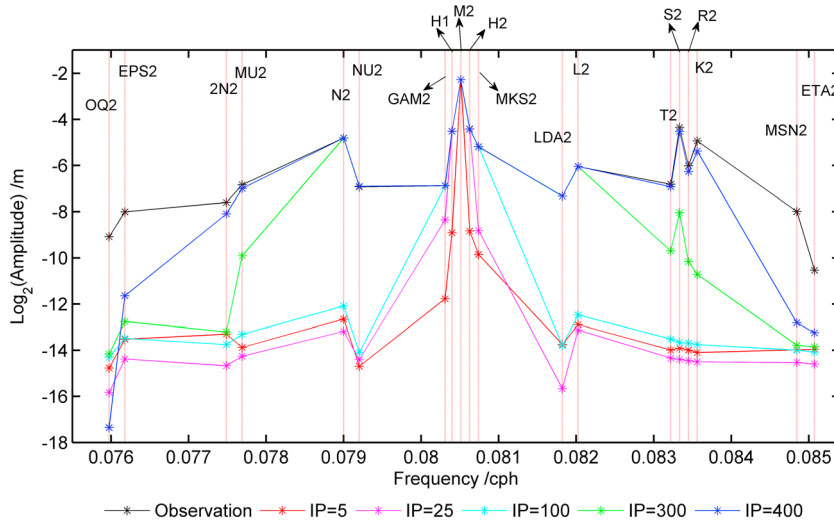


**Figure 9.** Amplitudes of constituents in D<sub>2</sub> tidal bands by analyzing (using T\_TIDE) the observations and the hindcast of S\_TIDE with different IP numbers for major constituents (IP number for MWL was set to 1,500). IP = independent point; MWL = mean water level.

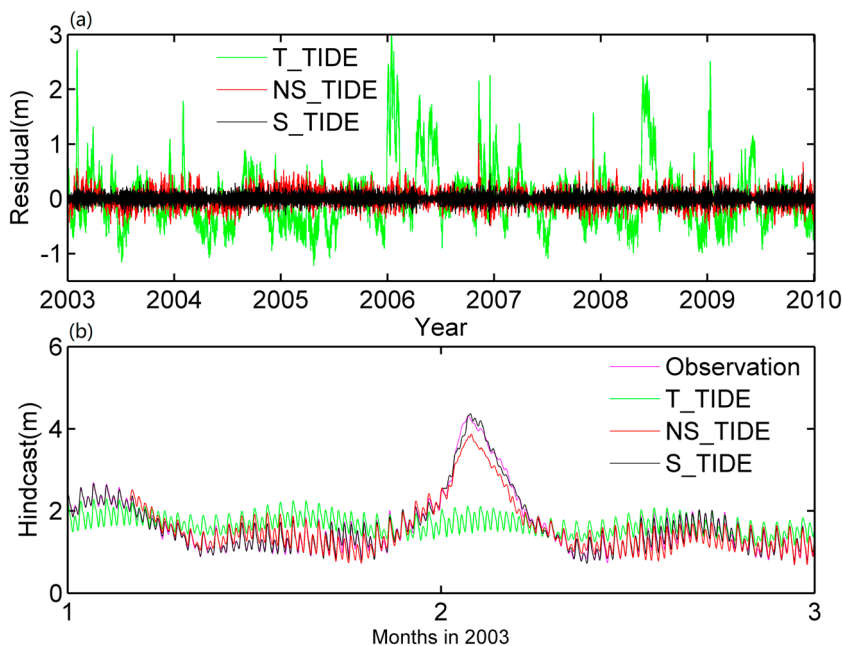


**Figure 10.** (a) Residuals for T\_TIDE, NS\_TIDE ( $\eta = 0.15$ ), and S\_TIDE (IP = 400) at Vancouver from January 2003 to December 2009; (b) Hindcasts by T\_TIDE, NS\_TIDE ( $\eta = 0.15$ ), and S\_TIDE (IP = 400) as well as observations at Vancouver from January 2003 to March 2003. IP = independent point.

constituents a posteriori to exclude those that are not significant. For example, in NS\_TIDE, when the parameter  $\eta$  for the redefined Rayleigh criterion is set to 0.15, there are seven constituents (EPS<sub>2</sub>, MU<sub>2</sub>, N<sub>2</sub>, M<sub>2</sub>, L<sub>2</sub>, S<sub>2</sub>, and MSN<sub>2</sub>) that can be resolved in D<sub>2</sub> tidal band. Since MU<sub>2</sub> is adjacent to N<sub>2</sub>, they cannot be extracted with the IP scheme simultaneously. But considering that N<sub>2</sub> is more important (based on a similar decision tree as in NS\_TIDE), we exclude MU<sub>2</sub>. L<sub>2</sub> can also be excluded in the same way. Therefore, in S\_TIDE, only five constituents (EPS<sub>2</sub>, N<sub>2</sub>, M<sub>2</sub>, S<sub>2</sub>, and MSN<sub>2</sub>) can be resolved in D<sub>2</sub> tidal band. But note that the premise that these five constituents can be resolved in S\_TIDE is the IP numbers for these constituents must be strictly limited. If the IP number for M<sub>2</sub> is 400, it is obvious that only M<sub>2</sub> can be resolved in D<sub>2</sub> tidal band by S\_TIDE.

#### 3.4.4. Performance of S\_TIDE

In this section, NS\_TIDE and S\_TIDE will be compared in details when applied to Vancouver. In NS\_TIDE, we use  $\eta = 0.15$  with optimized exponents (cf. equation (8)). In S\_TIDE, eight constituents (K<sub>1</sub>, M<sub>2</sub>, MK<sub>3</sub>, M<sub>4</sub>, 2MK<sub>5</sub>, M<sub>6</sub>, 3MK<sub>7</sub>, and M<sub>8</sub>) are selected. The IP number for these constituents was set to 400, and the IP number for MWL was set to 1,500.

S\_TIDE performs better than NS\_TIDE: the hindcast obtained by S\_TIDE accounts for 99.1% of the original signal variance and having a RMSE of 0.075 m and a MAE of 0.48 m. Figure 10 shows that the hindcast obtained by S\_TIDE is almost the same as the observation and its residual is extremely small. As indicated in the sensitivity experiments, a large part of the error in NS\_TIDE comes from the less accurate MWL inversed by NS\_TIDE compared to S\_TIDE.

Figure 11a shows the tides (D<sub>1</sub>-D<sub>8</sub>) obtained by S\_TIDE (IP = 400) and NS\_TIDE ( $\eta = 0.15$ ) at Vancouver. Tides obtained by S\_TIDE and NS\_TIDE have similar patterns with a correlation coefficient of 0.95. The red line, blue line, and black line in Figure 11b represent the difference of hindcast, tide, and MWL obtained by S\_TIDE (IP = 400) and NS\_TIDE ( $\eta = 0.15$ ) at Vancouver, respectively. As shown in Figure 11b, the red line and the black line have a similar pattern with a correlation coefficient of 0.93. While the correlation coefficient between the red line and the blue line only is 0.36. Figure 11b also indicates that the difference of hindcast obtained by S\_TIDE and NS\_TIDE is mainly derived from the difference of MWL.

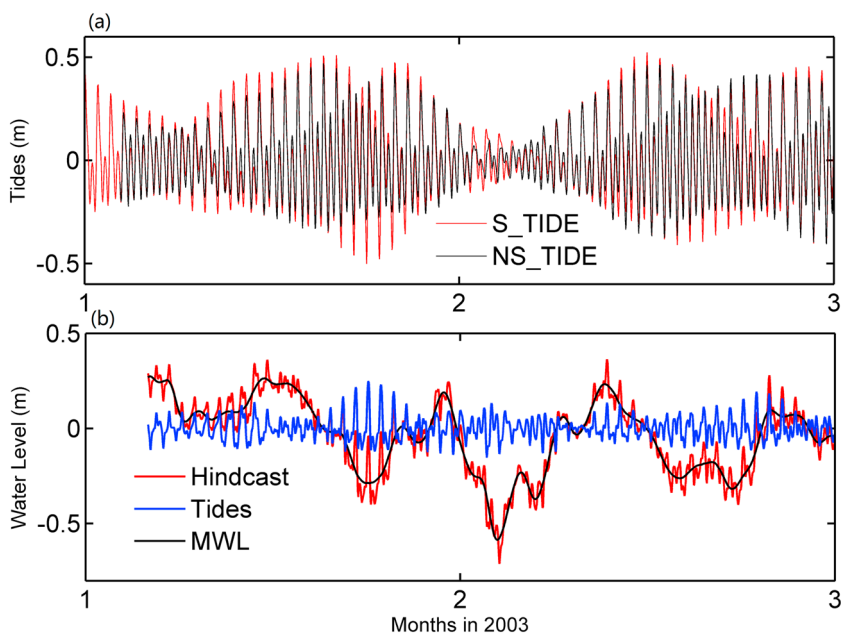


**Figure 11.** (a) Tides ( $D_1-D_8$ ) obtained by S\_TIDE ( $IP = 400$ ) and NS\_TIDE ( $\eta = 0.15$ ) at Vancouver from January 2003 to March 2003; (b) Differences of hindcast, tide, and MWL obtained by S\_TIDE ( $IP = 400$ ) and NS\_TIDE ( $\eta = 0.15$ ) at Vancouver from January 2003 to March 2003. IP = independent point; MWL = mean water level.

## 4. Discussions

### 4.1. Application of S\_TIDE to Other Stations in the Columbia River

Other stations in the LCR are also analyzed to evaluate our method and study the along-channel tidal-fluvial process. The settings of NS\_TIDE and S\_TIDE are the same as section 3.4.4 for all stations except Wauna. At Wauna station, the LORs is much shorter than those at other stations. The IP number for constituents decreases to 229, and the IP number for MWL decreases to 915 according to the LOR.

As shown in Table 5, the performance of S\_TIDE is better than NS\_TIDE in all stations in the LCR. Although both methods explain most of the original signal variance, S\_TIDE improves the RMSE by a few centimeters compared to NS\_TIDE. More importantly, S\_TIDE captures the extrema better than NS\_TIDE, thus significantly reducing the MAE. It is interesting, however, that S\_TIDE becomes slightly less accurate moving downriver, but the reason is unknown.

Adding the CUI in NS\_TIDE at Vancouver only improves marginally the percent explained variance (~0.1%) and RMSE (<1 cm), with an improved MAE of about 2 cm (see Table S2 in the supporting information). However, the impact of the CUI is expected to increase seaward (Table S2), where it improves the MAE by 8, 9, and 12 cm at St. Helens, Longview, and Wauna, respectively. When looking more closely at the tidal datum levels (not shown), MWLs are improved by up to 5 cm during peak downwelling events, while HHW and LLW can be improved by 20–30 cm. These results are in line with those of Jay et al. (2016) and highlight

**Table 5**

*The Performance of NS\_TIDE and S\_TIDE on Water Level Records in the Lower Columbia River*

Station	NS_TIDE			S_TIDE		
	Signal variance (%)	RMSE (m)	MAE (m)	Signal variance (%)	RMSE (m)	MAE (m)
Wauna (rkm 68)	96.2	0.131	1.014	97.2	0.114	0.745
Longview (rkm 107)	94.6	0.133	1.011	98.0	0.083	0.561
St. Helens (rkm 139)	94.8	0.142	1.013	98.9	0.070	0.413

Note. MWL = mean water level; RMSE = root-mean-square error; rkm = river kilometers.

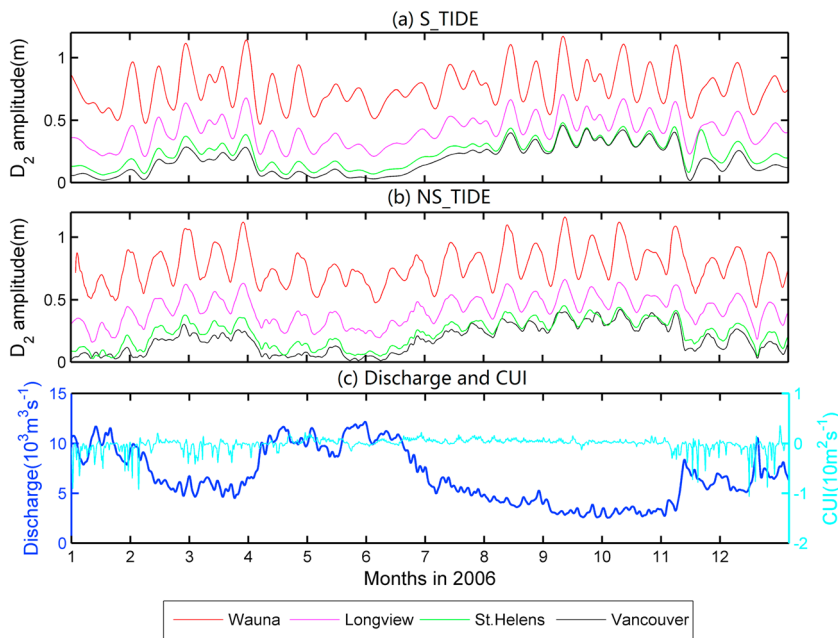


**Figure 12.** (a)  $D_2$  amplitude obtained by S\_TIDE from January 2006 to December 2006. (b) Same as Figure 12a but obtained by NS\_TIDE. (c) Discharge in the lower Columbia River from January 2006 to December 2006 (sum of river flows at Bonneville dam and from the Willamette River) and CUI at 46°N. CUI = Coastal Upwelling Index.

the fact that CUI not only affects MWL, but its effects on HHW and LLW, expressed via the tidal-fluvial model in NS\_TIDE, are even more pronounced.

As displayed in Figure 12, the  $D_2$  amplitudes obtained by S\_TIDE and NS\_TIDE are similar and highly agree with the tidal-fluvial model established by Kukulka and Jay (2003a). As tides propagate upriver, they are gradually distorted and damped (Jay, 1991; Matte et al., 2013). Thus, the more landward a station is, the smaller its  $D_2$  amplitude is (Figure 12). The  $D_2$  amplitudes obtained by the two methods at all stations increase as the discharge decreases. From August 2006 to November 2006, fortnightly oscillations in  $D_2$  amplitudes obtained by S\_TIDE at all stations become stronger as the river flow decreases. It should be noted that the amplitudes obtained by S\_TIDE are very smooth due to application of cubic spline interpolation, while the amplitudes obtained by NS\_TIDE are not smooth and contain many weak oscillations that are derived from discharge. In NS\_TIDE, amplitudes and phases are functions of river flow and tidal forcing. Therefore, any small change in river flow can be reflected by the amplitudes and phases. In this respect NS\_TIDE is superior.

Time-space variations of  $D_1$  amplitudes are similar to those of  $D_2$  amplitudes (Figure 13). The overtides, on the other hand, derive mostly from nonlinear frictional interactions rather than astronomical forcing; thus, the along-channel variations of overtide amplitudes are different from those of  $D_1$  and  $D_2$  (Figure 13). As indicated by Jay et al. (2015), overtides  $MK_3$  and  $M_4$  are small in the Columbia estuary but increase upriver to a maximum at Beaver (rkm 87) and then decrease upriver.  $M_4$  amplitudes are nearly equal at Wauna (rkm 68) and Longview (rkm 107). However, the classical HA that is used in Jay et al. (2015) only provides time-averaged values of constituents amplitude. As shown in Figures 13c and 13d, during the first half year of 2006,  $D_4$  amplitudes at Wauna are larger than those at Longview, while in the second half year of 2006,  $D_4$  amplitudes at Wauna are smaller than those at Longview. As displayed in Figures 14c and 14d, the difference of  $D_4$  amplitudes between Wauna and Longview is mainly influenced by river flow with a correlation coefficient of 0.90. As river flow increases,  $D_4$  amplitudes at Wauna are larger than those at Longview, and vice versa. Therefore, for  $D_4$  constituents, not only the time variations but also the along-channel variations are dominated by river flow. The correlation coefficient between river flow and the difference of  $D_1$  amplitudes between Wauna and Longview are 0.40. For  $D_1$  constituents, the time variations are dominated by river flow, and the along-channel variations are also slightly influenced by river flow. The correlation

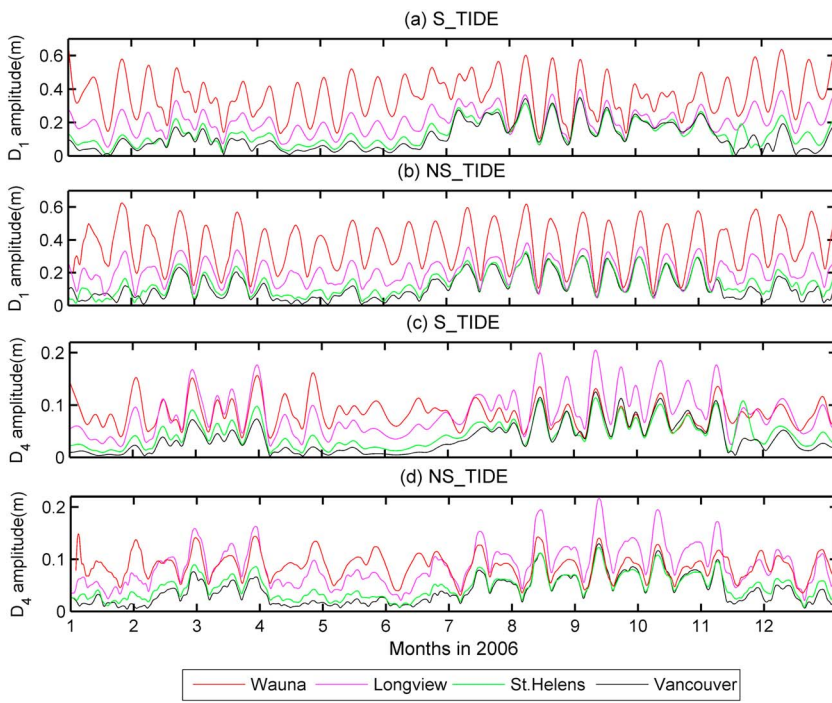


**Figure 13.** (a)  $D_1$  amplitude obtained by S\_TIDE from January 2006 to December 2006. (b) Same as Figure 13a but obtained by NS\_TIDE. (c) Same as Figure 13a but for  $D_4$  amplitude. (d) Same as Figure 13c but obtained by NS\_TIDE.

coefficient between river flow and the difference of  $D_2$  amplitudes between Wauna and Longview are 0.27. For  $D_2$  constituents, the time variations are dominated by river flow, but the along-channel variations are only weakly influenced by river flow. The  $D_4$  amplitudes are far smaller than  $D_1$  and  $D_2$  amplitudes. Thus, the  $D_4$  constituents are most easily altered by discharge when propagating upriver. As also observed by

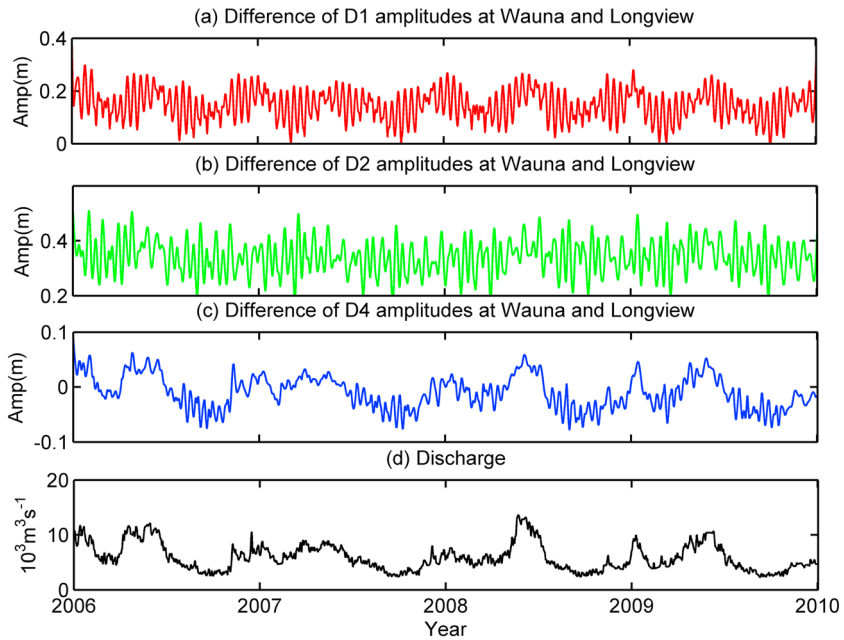


**Figure 14.** (a) Difference of  $D_1$  amplitudes at Wauna and Longview obtained by S\_TIDE from January 2006 to December 2009. (b) Same as Figure 14a but for  $D_2$  amplitudes. (c) Same as Figure 14a but for  $D_4$  amplitudes. (d) Discharge in the lower Columbia River from January 2006 to December 2009 (sum of river flows at Bonneville dam and from the Willamette River).

Matte et al. (2014), overtides are generated through nonlinear interactions of the principal tides with friction and river flow, until they reach a point upstream where they are damped more rapidly than they are generated.

#### 4.2. Advantages and Disadvantages of S\_TIDE

##### 4.2.1. Advantages of S\_TIDE

1. Compared to CWT and NS\_TIDE, S\_TIDE is simple and easy to implement. The results obtained by S\_TIDE are similar to EMD, CWT, and NS\_TIDE, and highly consistent with theory on river tides. Compared to NS\_TIDE, the hindcast obtained with S\_TIDE is more accurate.
2. Like conventional HA, S\_TIDE is free of dynamic content, assuming only known tidal frequencies. S\_TIDE does not rely on the availability of river flow records, which makes it easily transposable to any nonstationary tidal context (e.g., internal tides). Furthermore, although S\_TIDE is designed for nonstationary tides, our method can also be applied to stationary tides to analyze secular changes of tidal amplitude and sea level simultaneously.
3. As demonstrated in section 3.4.2, S\_TIDE and EMD could play a role of low-pass filter. Compared to S\_TIDE, the shortcoming of EMD is that it is a nonparametric method. Each EMD mode is not restricted to a narrowband signal, and it can be both amplitude and frequency modulated; that is, its amplitude and frequency are functions of time, and thus, it cannot guarantee extraction of the known tidal constituents (Pan et al., 2018). We can use S\_TIDE to separate tidal parts from subtidal parts of water level records accurately. We can also use S\_TIDE to separate oscillations in MWL, amplitudes, and phases on different time scales.

##### 4.2.2. Disadvantages of S\_TIDE

1. Compared to NS\_TIDE, S\_TIDE can only be a powerful time series analysis method like EMD. NS\_TIDE can be used for prediction, while S\_TIDE and EMD cannot. This is a significant drawback of S\_TIDE. In this regard, NS\_TIDE may be the only method that can provide effective and relatively precise prediction of river tides, unless the other methods are used within a similar framework as Kukulka and Jay's (2003a, 2003b) for CWT. Also, as indicated in section 4.1, results obtained by NS\_TIDE can reflect small changes in river flow, while S\_TIDE cannot.
2. S\_TIDE needs more computation resources and computation time than other methods when the number of IPs is large. For example, as indicated in equation (8), NS\_TIDE uses 14 constants per constituent (ten polynomial coefficients and four exponents) plus 9 constants for the subtidal part. However, to gain the best performance, S\_TIDE uses 800 constants per constituent (400 IPs each for amplitude and phase) plus 1,500 constants for the subtidal part. For constituents used in section 4.1, in order to analyze hourly water level data for a 7-year period, NS\_TIDE employs 457 constants, while S\_TIDE uses 7,900 constants, an exceptionally large number for a tidal model. The number of constants in S\_TIDE is 17.3 times that used in NS\_TIDE. In the subtidal model, the number of constants in S\_TIDE is 166.7 times that used in NS\_TIDE. This explains the relative success of S\_TIDE: it is not surprising that 7,900 constants do a better job than 457 constants in describing the same data. However, this success is realized at the cost of more computation resources and computation time. Also, too many IPs in S\_TIDE may induce computational memory overflow and unrealistic results. For example, when the IP number for constituents exceeds 500, the neap spring oscillations in amplitudes are obviously exaggerated due to overfitting. Therefore, it should be noted that S\_TIDE is not like a *point and shoot* camera. Caution should be exercised during selecting constituents and IPs.

### 5. Conclusions

Based on the IP scheme and cubic spline interpolation, a new approach, EHA, was developed to deal with nonstationary tides. EHA is realized by a MATLAB toolbox, S\_TIDE, which is developed from the widely used T\_TIDE. S\_TIDE assumes only known tidal frequencies and theoretically can be applied to all kinds of nonstationary tides and stationary tides. Although EHA was first proposed by Jin et al. (2018), they did not clarify how to select IP numbers for EHA due to the limited observations and complicated physical process. In this study, S\_TIDE is applied to analyzing records of river tides that is one of the simplest kinds of nonstationary tides for which ample data are available. The method is compared with T\_TIDE, CWT, EMD, and NS\_TIDE to show its efficiency. Results indicate that S\_TIDE performs better than T\_TIDE and NS\_TIDE with the smallest residual and shows an advantage in the hindcast of water level. Also, a series of

sensitivity experiments were carried out to discuss the selection of the numbers of IPs in detail. It was first found that MWL, amplitudes, and phases obtained by S\_TIDE with different IP numbers represent oscillations on different time scales. However, there is a trade-off between the numbers of constituents included in S\_TIDE and the number of IPs for constituents. In summary, although S\_TIDE cannot be used for prediction, it has the potential to be used in future studies of the nonlinear, time-dependent dynamics of estuaries and coastal seas.

## Appendix A: Theoretical Models of River Tides

Kukulka and Jay (2003a) proposed the tidal-fluvial model

$$\ln \left[ \frac{\varsigma(x)}{\varsigma_0} \right] = b_0 + b_1 Q^p + b_2 \frac{R^q}{Q^r} \quad (A1)$$

where  $\varsigma(x)$  represents a tidal property at position  $x$ ,  $\varsigma_0$  is the same property at the reference station,  $Q$  is the river discharge, and  $R$  is the greater diurnal tidal range at the reference station. Equation (A1) indicates that the tidal properties at the station of interest are nonlinear functions of streamflow and tidal forcing at the reference station. The discharge term  $b_1 Q^p$  represents the nonlinear effect of the river flow. The coefficient  $b_1$  is negative in general; hence, the amplitude decreases when discharge increases.  $b_2 \frac{R^q}{Q^r}$  is the tidal range term representing the nonlinear tidal-fluvial interaction due to neap-spring variability. The range term becomes less important as discharge increases. As indicated by Kukulka and Jay (2003a), the theoretical values of  $p$ ,  $q$ , and  $r$  are 1, 2, and 0.5, respectively. But, in fact, the  $Q$  in equation (A1) is a simplification—in theory,  $U = Q/A(Q)$  should be used, where  $A(Q)$  represents the cross-sectional area. The variations of  $A$  with river flow can cause deviations of exponent  $p$  from theory. Also, theoretical values of  $q$  are valid only for stations where river flow and tidal currents are of similar magnitude (Matte et al., 2013).

In practice, a simplification is applied using the first term in the Taylor expansion of  $\ln[\varsigma(x)/\varsigma_0]$ :

$$\ln \left[ \frac{\varsigma(x)}{\varsigma_0} \right] = \ln \left[ 1 - \frac{\varsigma_0 - \varsigma(x)}{\varsigma_0} \right] \approx \frac{\varsigma_0 - \varsigma(x)}{\varsigma_0} \quad (A2)$$

Thus, equation (A1) can be rewritten as

$$\varsigma(x) = c_0 + c_1 Q^p + c_2 \frac{R^q}{Q^r} \quad (A3)$$

Kukulka and Jay (2003b) also developed the stage model

$$s(x) = d_0 + d_1 Q^p + d_2 \frac{R^q}{Q^r} + d_{\text{pre}} \Delta p_{\text{atm}} \quad (A4)$$

where  $s(x)$  represents the MWL at position  $x$ . Compared with equation (A3), equation (A4) has an additional atmospheric pressure term,  $d_{\text{pre}} \Delta p_{\text{atm}}$ . As indicated by Kukulka and Jay (2003b),  $p$ ,  $q$ , and  $r$  are theoretically 0.67, 2, and 1.33, respectively.

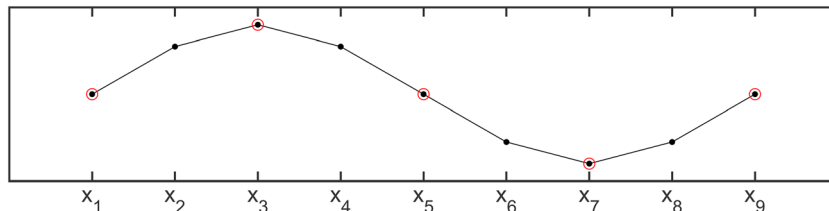


**Figure A1.** Sketch illustrates the IP scheme. The  $x$  axis has labels of  $x_1$  on the left to  $x_9$  on the right. IP = independent point.

## Appendix B: Computation of Cubic Spline Interpolation Weights

The cubic spline  $S(x)$  on the interval  $[x_i, x_{i+1}]$  between two adjacent IPs, for which

$$\begin{cases} S(x_i) = y_i, S(x_{i+1}) = y_{i+1} (i = 0, 1, 2, \dots, n) \\ S'(x_i) = m_i, S'(x_{i+1}) = m_{i+1} (i = 0, 1, 2, \dots, n) \end{cases} \quad (\text{B1})$$

can be written as

$$\begin{aligned} S(x) &= \left(\frac{x - x_{i+1}}{h_i}\right)^2 \left(1 + 2\frac{x - x_i}{h_i}\right) y_i + \left(\frac{x - x_i}{h_i}\right)^2 \left(1 - 2\frac{x - x_{i+1}}{h_i}\right) y_{i+1} \\ &\quad + \left(\frac{x - x_{i+1}}{h_i}\right)^2 (x - x_i) m_i + \left(\frac{x - x_i}{h_i}\right)^2 (x - x_{i+1}) m_{i+1} \\ &\quad (h_i = x_{i+1} - x_i, x_i \leq x \leq x_{i+1}) \end{aligned} \quad (\text{B2})$$

Continuity of the second derivative of  $S(x)$  at point  $x_i$  requires that

$$S''(x_i^+) = S''(x_i^-), (i = 1, 2, \dots, n - 1) \quad (\text{B3})$$

that is,

$$-\frac{6(y_1 - y_{i-1})}{h_{i-1}^2} + \frac{2m_{i-1} + 4m_i}{h_{i-1}} = \frac{6(y_{i+1} - y_i)}{h_i^2} - \frac{4m_i + 2m_{i+1}}{h_i} \quad (\text{B4})$$

Equation (B4) can be simplified as

$$(1 - \alpha_i)m_{i-1} + 2m_i + \alpha_i m_{i+1} = \beta_i (i = 1, 2, \dots, n - 1) \quad (\text{B5})$$

where

$$\alpha_i = \frac{h_{i-1}}{h_{i-1} + h_i}, \beta_i = 3 \left[ \frac{1 - \alpha_i}{h_{i-1}} (y_i - y_{i-1}) + \frac{\alpha_i}{h_i} (y_{i+1} - y_i) \right] \quad (\text{B6})$$

In this paper, IPs are uniformly distributed, namely

$$h_i = h_{i-1} = h \quad (\text{B7})$$

Thus, equation (B6) can be simplified as

$$\alpha_i = \frac{1}{2}, \beta_i = \frac{3}{2h} (y_{i+1} - y_{i-1}) \quad (\text{B8})$$

Additional boundary conditions are required to determine cubic spline functions. In S\_TIDE, we adopt common natural boundary condition:

$$S''(x_0) = S''(x_n) = 0 \quad (\text{B9})$$

that is,

$$\begin{cases} 2m_0 + m_1 = \frac{3}{h} (y_1 - y_0) \\ m_{n-1} + 2m_n = \frac{3}{h} (y_n - y_{n-1}) \end{cases} \quad (\text{B10})$$

We can get from equations (B5) and (B10) that

$$AM = Y \quad (\text{B11})$$

where

$$A = \begin{bmatrix} 1 & 0.5 & 0 & 0 & \cdots & 0 & 0 & 0 & 0 \\ 0.5 & 2 & 0.5 & 0 & \cdots & 0 & 0 & 0 & 0 \\ 0 & 0.5 & 2 & 0.5 & \cdots & 0 & 0 & 0 & 0 \\ 0 & 0 & 0.5 & 2 & \cdots & 0 & 0 & 0 & 0 \\ \cdots & \cdots \\ 0 & 0 & 0 & 0 & \cdots & 2 & 0.5 & 0 & 0 \\ 0 & 0 & 0 & 0 & \cdots & 0.5 & 2 & 0.5 & 0 \\ 0 & 0 & 0 & 0 & \cdots & 0 & 0.5 & 2 & 0.5 \\ 0 & 0 & 0 & 0 & \cdots & 0 & 0 & 0.5 & 1 \end{bmatrix} \quad M = \begin{bmatrix} m_0 \\ m_1 \\ m_2 \\ m_3 \\ \vdots \\ m_{n-3} \\ m_{n-2} \\ m_{n-1} \\ m_n \end{bmatrix} \quad Y = \frac{3}{2h} \begin{bmatrix} y_1 - y_0 \\ y_2 - y_0 \\ y_3 - y_1 \\ y_4 - y_2 \\ \vdots \\ y_{n-2} - y_{n-4} \\ y_{n-1} - y_{n-3} \\ y_n - y_{n-2} \\ y_n - y_{n-1} \end{bmatrix} \quad (B12)$$

set

$$C = \begin{bmatrix} -1 & 1 & 0 & 0 & \cdots & 0 & 0 & 0 & 0 \\ -1 & 0 & 1 & 0 & \cdots & 0 & 0 & 0 & 0 \\ 0 & -1 & 0 & 1 & \cdots & 0 & 0 & 0 & 0 \\ 0 & 0 & -1 & 0 & \cdots & 0 & 0 & 0 & 0 \\ \cdots & \cdots \\ 0 & 0 & 0 & 0 & \cdots & 0 & 1 & 0 & 0 \\ 0 & 0 & 0 & 0 & \cdots & -1 & 0 & 1 & 0 \\ 0 & 0 & 0 & 0 & \cdots & 0 & -1 & 0 & 1 \\ 0 & 0 & 0 & 0 & \cdots & 0 & 0 & -1 & 1 \end{bmatrix} \quad y = \begin{bmatrix} y_0 \\ y_1 \\ y_2 \\ y_3 \\ \vdots \\ y_{n-3} \\ y_{n-2} \\ y_{n-1} \\ y_n \end{bmatrix} \quad (B13)$$

$$B = \frac{3}{2h} A^{-1} C \quad (B14)$$

We can get from equations (B11) and (B14) that

$$M = A^{-1} Y = B y \quad (B15)$$

Combination of equations (B2) and (B15) yields equation (B16)

$$S(x) = f y \quad (B16)$$

where  $f$  is the cubic spline interpolation weights.

$f$  at the  $k$ th point in the interval  $[x_i, x_{i+1}]$  of the  $l$ th IP can be expressed as

$$f_{k,l} = \begin{cases} \left(\frac{k-x_{i+1}}{h}\right)^2 \left(1 + 2\frac{k-x_i}{h}\right) + \tilde{f}_{k,l} & (l=i, l \neq i+1) \\ \tilde{f}_{k,l} & (l \neq i, l \neq i+1) \\ \left(\frac{k-x_i}{h}\right)^2 \left(1 - 2\frac{k-x_{i+1}}{h}\right) + \tilde{f}_{k,l} & (l=i+1) \end{cases} \quad (B17)$$

where

$$\tilde{f}_{k,l} = \left(\frac{k-x_{i+1}}{h}\right)^2 (k-x_i)B_{i,l} + \left(\frac{k-x_i}{h}\right)^2 (k-x_{i+1})B_{i+1,l} \quad (B18)$$

### Appendix C: The Performance of S\_TIDE With the Linear Interpolation

Guo et al. (2018) choose the linear interpolation in the IP scheme because it will not produce significant artificial oscillations and it is simple in terms of computation (compared to the cubic spline interpolation). But the major limitation of the linear interpolation is that the obtained MWL, amplitude, and phase are not smooth.

Here we conduct experiments to compare the performance of cubic spline interpolation with the linear interpolation. The IP numbers for constituents (only considers  $M_2$  and  $K_1$ ) are set to 25, and the IP numbers for MWL are set to 1,500. As shown in Figure S2, the MWL and  $M_2$  amplitude at Vancouver obtained by S\_TIDE with two interpolation methods are highly similar. The results obtained by the cubic spline interpolation are smooth, while the results obtained by the linear interpolation are not smooth. The hindcast of S\_TIDE (using the cubic spline interpolation) accounts for 97.3% of the original signal variance with a RMSE of 0.13 m and a MAE of 0.60 m, while the hindcast of S\_TIDE (using the linear interpolation) accounts for 97.2% of the original signal variance with a RMSE of 0.13 m and a MAE of 0.74 m. The performance of S\_TIDE using the cubic spline interpolation is slightly better than the linear interpolation.

### Acknowledgments

The authors deeply thank the reviewers and Editor for their constructive criticism of an early version of the manuscript. Tide data were provided by the National Oceanic and Atmospheric Administration (<https://tidesandcurrents.noaa.gov>). Flow data were provided by the U.S. Geological Survey (<https://nwis.waterdata.usgs.gov/nwis>). CUI data were obtained from NOAA (<https://www.pfeg.noaa.gov/products/PFELmodeled/indices/upwelling/>). The authors thank Pascal Matte, David A. Jay, and Edward D. Zaron for providing the NS\_TIDE package and data. The authors thank Rich Pawlowicz, Bob Beardsley, and Steve Lentz for distributing the T\_TIDE package. The authors also thank G. Rilling for distributing the EMD package. Thanks are extended to Yongzhi Liu, Anzhou Cao, Zheng Guo, and Daosheng Wang for their friendly help on the paper. Partial support for this research was provided by the National Key Research and Development Plan through grant 2016YFC1402304, the National Natural Science Foundation of China through grant 41606006, the Key Research and Development Plan of Shandong Province through grant 2016ZDJ509A02, and the Fundamental Research Funds for the Central Universities. S\_TIDE package is available upon request ([panhaidong\\_phd@qq.com](mailto:panhaidong_phd@qq.com)). New version of NS\_TIDE package is also available upon request ([pascal.matte@canada.ca](mailto:pascal.matte@canada.ca)).

### References

- Bottom, D. L., Simenstad, C. A., Burke, J., Baptista, A. M., Jay, D. A., Jones, K. K., et al. (2005), Salmonon river's end: The role of the estuary in the decline and recovery of Columbia River salmon, NOAA Tech. Memo.NMFS-NWFSC-68, 246 pp.
- Cheng, Y., Ezer, T., Atkinson, L. P., & Xu, Q. (2017). Analysis of tidal amplitude changes using the EMD method. *Continental Shelf Research*, 148, 44–52. <https://doi.org/10.1016/j.csr.2017.09.009>
- Cheng, Y., Ezer, T., & Hamlington, B. (2016). Sea level acceleration in the China seas. *Water*, 8(7), 293. <https://doi.org/10.3390/w8070293>
- Ezer, T. (2013). Sea level rise, spatially uneven and temporally unsteady: Why the U.S. East Coast, the global tide gauge record, and the global altimeter data show different trends. *Geophysical Research Letters*, 40, 5439–5444. <https://doi.org/10.1002/2013GL057952>
- Ezer, T., & Corlett, W. B. (2012). Is sea level rise accelerating in the Chesapeake Bay? A demonstration of a novel new approach for analyzing sea level data. *Geophysical Research Letters*, 39, L19605. <https://doi.org/10.1029/2012GL053435>
- Ezer, T., Haigh, I. D., & Woodworth, P. L. (2016). Nonlinear sea-level trends and long-term variability on western European coasts. *Journal of Coastal Research*, 320, 744–755. <https://doi.org/10.2112/JCOASTRES-D-15-00165.1>
- Familkhilii, R., & Talke, S. A. (2016). The effect of channel deepening on tides and storm surge: A case study of Wilmington, NC. *Geophysical Research Letters*, 43, 9138–9147. <https://doi.org/10.1002/2016GL069494>
- Flandrin, P., Rilling, G., & Goncalves, P. (2004). Empirical mode decomposition as a filter bank. *IEEE Signal Processing Letters*, 11(2), 112–114. <https://doi.org/10.1109/LSP.2003.821662>
- Foreman, M. G. G., & Henry, R. F. (1989). The harmonic analysis of tidal model time series. *Advances in Water Resources*, 12(3), 109–120. [https://doi.org/10.1016/0309-1708\(89\)90017-1](https://doi.org/10.1016/0309-1708(89)90017-1)
- Godin, G. (1972). *The Analysis of Tides* (p. 264). Toronto, Canada: University of Toronto Press.
- Guo, L., van der Wegen, M., Jay, D. A., Matte, P., Wang, Z. B., Roelvink, D., & He, Q. (2015). River-tide dynamics: Exploration of nonstationary and nonlinear tidal behavior in the Yangtze River estuary. *Journal of Geophysical Research: Oceans*, 120, 3499–3521. <https://doi.org/10.1002/2014JC010491>
- Guo, Z., Pan, H., Cao, A., & Lv, X. (2018). A harmonic analysis method adapted to capturing slow variations of tidal amplitudes and phases. *Continental Shelf Research*, 164, 37–44. <https://doi.org/10.1016/j.csr.2018.06.005>
- Guo, Z., Pan, H., Fan, W., & Lv, X. (2017). Application of surface spline interpolation in inversion of bottom friction coefficients. *Journal of Atmospheric and Oceanic Technology*, 34(9), 2021–2028. <https://doi.org/10.1175/JTECH-D-17-0012.1>
- Hoitink, A. J. F., & Jay, D. A. (2016). Tidal river dynamics: Implications for deltas. *Reviews of Geophysics*, 54, 240–272. <https://doi.org/10.1002/2015RG000507>
- Huang, N. E., Shen, Z., Long, S. R., Wu, M. C., Shih, H. H., Yen, N., et al. (1998). The empirical mode decomposition and the Hilbert spectrum for nonlinear and non-stationary time series analysis. *Royal Society Publication*, 454(1971), 903–995. <https://doi.org/10.1098/rspa.1998.0193>
- Huber, P. J. (1996). Robust statistical procedures. In *CBMS-NSF regional conference series in applied mathematics* (2nd ed., Vol. 68, p. 67). Philadelphia, PA: Society of Industrial and Applied Mathematics.
- Jay, D. A. (1991). Green's law revisited: Tidal long-wave propagation in channels with strong topography. *Journal of Geophysical Research*, 96(C11), 20585. <https://doi.org/10.1029/91JC01633>
- Jay, D. A., Borde, A. B., & Diefenderfer, H. L. (2016). Tidal-fluvial and estuarine processes in the lower Columbia River: II. Water level models, floodplain wetland inundation, and system zones. *Estuaries and Coasts*, 39(5), 1299–1324. <https://doi.org/10.1007/s12237-016-0082-4>
- Jay, D. A., & Flincham, E. P. (1997). Interaction of fluctuating river flow with a barotropic tide: A demonstration of wavelet tidal analysis methods. *Journal of Geophysical Research*, 102(C3), 5705–5720. <https://doi.org/10.1029/96JC00496>
- Jay, D. A., & Flincham, E. P. (1999). A comparison of methods for analysis of tidal records containing multi-scale non-tidal background energy. *Continental Shelf Research*, 19(13), 1695–1732. [https://doi.org/10.1016/S0278-4343\(99\)00036-9](https://doi.org/10.1016/S0278-4343(99)00036-9)
- Jay, D. A., & Kukulka, T. (2003). Revising the paradigm of tidal analysis—The uses of non-stationary data. *Ocean Dynamics*, 53(3), 110–125. <https://doi.org/10.1007/s10236-003-0042-y>
- Jay, D. A., Lefler, K., & Degens, S. (2011). Long-term evolution of Columbia River tides. *Journal of Waterway Port, Coastal, and Ocean Engineering*, 137(4), 182–191. [https://doi.org/10.1061/\(ASCE\)WW.1943-5460.0000082](https://doi.org/10.1061/(ASCE)WW.1943-5460.0000082)

- Jay, D. A., Leffler, K., Diefenderfer, H. L., & Borde, A. B. (2015). Tidal-fluvial and estuarine processes in the lower Columbia River: I. Along-channel water level variations, Pacific Ocean to Bonneville dam. *Estuaries and Coasts*, 38(2), 415–433. <https://doi.org/10.1007/s12237-014-9819-0>
- Jin, G., Pan, H., Zhang, Q., Lv, X., Zhao, W., & Gao, Y. (2018). Determination of harmonic parameters with temporal variations: An enhanced harmonic analysis algorithm and application to internal tidal currents in the South China Sea. *Journal of Atmospheric and Oceanic Technology*, 35(7), 1375–1398. <https://doi.org/10.1175/JTECH-D-16-0239.1>
- Kukulka, T., & Jay, D. A. (2003a). Impacts of Columbia River discharge on salmonid habitat: 1. A nonstationary fluvial tide model. *Journal of Geophysical Research*, 108(C9), 3293. <https://doi.org/10.1029/2002JC001382>
- Kukulka, T., & Jay, D. A. (2003b). Impacts of Columbia River discharge on salmonid habitat: 2. Changes in shallow-water habitat. *Journal of Geophysical Research*, 108(C9), 3294. <https://doi.org/10.1029/2003JC001829>
- Leffler, K. E., & Jay, D. A. (2009). Enhancing tidal harmonic analysis: Robust (hybrid L1/L2) solutions. *Continental Shelf Research*, 29(1), 78–88. <https://doi.org/10.1016/j.csr.2008.04.011>
- Losada, M. A., Díez-Minguito, M., & Reyes-Merlo, M. (2017). Tidal-fluvial interaction in the Guadalquivir River estuary: Spatial and frequency-dependent response of currents and water levels. *Journal of Geophysical Research: Oceans*, 122, 847–865. <https://doi.org/10.1002/2016JC011984>
- Lu, X., & Zhang, J. (2006). Numerical study on spatially varying bottom friction coefficient of a 2D tidal model with adjoint method. *Continental Shelf Research*, 26(16), 1905–1923. <https://doi.org/10.1016/j.csr.2006.06.007>
- MacMahan, J. (2016). Observations of oceanic-forced subtidal elevations in a convergent estuary. *Estuarine, Coastal and Shelf Science*, 181, 319–324. <https://doi.org/10.1016/j.ecss.2016.09.002>
- Malik, R., Zhou, F., & Ceder, G. (2011). Kinetics of non-equilibrium lithium incorporation in LiFePO<sub>4</sub>. *Nature Materials*, 10(8), 587–590. <https://doi.org/10.1038/nmat3065>
- Matte, P., Jay, D. A., & Zaron, E. D. (2013). Adaptation of classical tidal harmonic analysis to nonstationary tides, with application to river tides. *Journal of Atmospheric and Oceanic Technology*, 30(3), 569–589. <https://doi.org/10.1175/JTECH-D-12-00016.1>
- Matte, P., Secretan, Y., & Morin, J. (2014). Temporal and spatial variability of tidal-fluvial dynamics in the St. Lawrence fluvial estuary: An application of nonstationary tidal harmonic analysis. *Journal of Geophysical Research: Oceans*, 119, 5724–5744. <https://doi.org/10.1002/2014JC009791>
- Moftakhi, H. R., Jay, D. A., & Talke, S. A. (2016). Estimating river discharge using multiple-tide gauges distributed along a channel. *Journal of Geophysical Research: Oceans*, 121, 2078–2097. <https://doi.org/10.1002/2015JC010983>
- Munk, W. H., Zetler, B., & Groves, G. W. (1965). Tidal cusps. *Geophysical Journal of the Royal Astronomical Society*, 10(2), 211–219. <https://doi.org/10.1111/j.1365-246X.1965.tb3062.x>
- Pan, H., Guo, Z., & Lv, X. (2017). Inversion of tidal open boundary conditions of the M2 constituent in the Bohai and Yellow Seas. *Journal of Atmospheric and Oceanic Technology*, 34(8), 1661–1672. <https://doi.org/10.1175/JTECH-D-16-0238.1>
- Pan, H., Guo, Z., Wang, Y., & Lv, X. (2018). Application of the EMD method to river tides. *Journal of Atmospheric and Oceanic Technology*, 35(4), 809–819. <https://doi.org/10.1175/JTECH-D-17-0185.1>
- Pawlowicz, R., Beardsley, B., & Lentz, S. (2002). Classical tidal harmonic analysis including error estimates in MATLAB using T\_TIDE. *Computational Geosciences*, 28(8), 929–937. [https://doi.org/10.1016/S0098-3004\(02\)00013-4](https://doi.org/10.1016/S0098-3004(02)00013-4)
- Sassi, M. G., & Hoitink, A. J. F. (2013). River flow controls on tides and tide-mean water level profiles in a tidal freshwater river. *Journal of Geophysical Research: Oceans*, 118, 4139–4151. <https://doi.org/10.1002/jgrc.2029>
- Wu, Z., & Huang, N. E. (2004). A study of the characteristics of white noise using the empirical mode decomposition method. *Proceedings of the Royal Society of London - Series A: Mathematical and Physical Sciences*, 460(2046), 1597–1611. <https://doi.org/10.1098/rspa.2003.1221>
- Zhang, J., Lu, X., Wang, P., & Wang, Y. P. (2011). Study on linear and nonlinear bottom friction parameterizations for regional tidal models using data assimilation. *Continental Shelf Research*, 31(6), 555–573. <https://doi.org/10.1016/j.csr.2010.12.011>